

AFGL 5180 and AFGL 6366S: sites of hub-filament systems at the opposite edges of a filamentary cloud

A. K. Maity^{1,2*}, L. K. Dewangan¹, N. K. Bhadari^{1,2}, D. K. Ojha³, Z. Chen⁴,
and Rakesh Pandey¹

¹Physical Research Laboratory, Navrangpura, Ahmedabad - 380 009, India.

²Indian Institute of Technology Gandhinagar Palaj, Gandhinagar 382355, India.

³Department of Astronomy and Astrophysics, Tata Institute of Fundamental Research, Homi Bhabha Road, Mumbai 400 005, India.

⁴Purple Mountain Observatory, Chinese Academy of Sciences Nanjing 210033, PR China.

ABSTRACT

We present a multi-scale and multi-wavelength study to unveil massive star formation (MSF) processes around sites AFGL 5180, and AFGL 6366S, both hosting a Class II 6.7 GHz methanol maser emission. The radio continuum map at 8.46 GHz reveals a small cluster of radio sources toward AFGL 5180. Signatures of the early stages of MSF in our target sites are spatially seen at the opposite edges of a filamentary cloud (length ~ 5 pc), which is observed in the sub-millimeter dust continuum maps. Using the near-infrared photometric data, the spatial distribution of young stellar objects is found toward the entire filament, primarily clustered at its edges. The *getsf* utility on the *Herschel* far-infrared images reveals a hub-filament system (HFS) toward each target site. The analysis of the molecular line data, which benefits from large area coverage ($\sim 1^\circ \times 1^\circ$), detects two cloud components with a connection in both position and velocity space. This supports the scenario of a cloud-cloud collision (CCC) that occurred ~ 1 Myr ago. The filamentary cloud, connecting AFGL 5180 and AFGL 6366S, seems spatially close to an H II region Sh2-247 excited by a massive O9.5 star. Based on the knowledge of various pressures exerted by the massive star on its surroundings, the impact of its energetic feedback on the filamentary cloud is found to be insignificant. Overall, our observational outcomes favor the possibility of the CCC scenario driving MSF and the formation of HFSs toward the target sites.

Key words: dust, extinction – H II regions – ISM: clouds – ISM: individual object (AFGL 5180 and AFGL 6366S) – stars: formation – stars: pre-main sequence

1 INTRODUCTION

Massive stars ($M \gtrsim 8 M_\odot$) are known for their tremendous radiative and mechanical feedback, which allow them to play a vital role in the evolution of their host galaxies (Bressert et al. 2012; Tremblin et al. 2014, and references therein). Despite their importance, the formation mechanism of massive stars is not yet fully understood (e.g., Zinnecker & Yorke 2007; Tan et al. 2014; Motte et al. 2018). In this relation, understanding the mass accumulation processes in massive star formation (MSF) is essential, which also includes the knowledge of the initial conditions of MSF. Hence, it requires extensive observational study of the surrounding environment involved in the early stages of MSF. The presence of massive stars is often evident through the detection of radio continuum emission from the H II regions (Sharpless 1959) and/or the detection of Class II 6.7 GHz methanol maser emission (MME; Menten 1991; Caswell et al. 1995; Walsh et al. 1998). Such proxies of MSF

are commonly observed toward the compact hub or dense region (Schneider et al. 2012; Tigé et al. 2017; Dewangan et al. 2017b, 2020b), which resides at the junction of several filaments (i.e., hub-filament systems (HFSs); Myers 2009). It is thought that MSF starts inside hot molecular cores. As it evolves, it drives a hyper-compact (HC) H II region (diameter (d) $\lesssim 0.05$ pc and electron density (n_e) $\gtrsim 10^5$ cm⁻³; Kurtz 2005; Yang et al. 2021) and then an ultra-compact (UC) H II region ($d \lesssim 0.1$ pc and $n_e \gtrsim 10^4$ cm⁻³; Churchwell 2002; Hoare et al. 2007). It is also believed that the 6.7 GHz MMEs exclusively trace the early stages of MSF (Minier et al. 2001; Breen et al. 2013). Such sites are very promising for probing the physical processes involved in the mass accumulation of MSF. In this context, the present paper deals with a target area hosting two potential massive star-forming regions, AFGL 5180 and AFGL 6366S, and each of them is associated with a 6.7 GHz MME.

The site AFGL 5180 is also known as G188.946+00.886 or IRAS 06058+2138 (hereafter, T1), while the region AFGL 6366S is referred to as G189.030+0.784 or IRAS 06056+2131 (hereafter, T2). Various distances have been reported to these sites in

* arupmaity@prl.res.in

the literature, which are 1.0–1.5 kpc (Bik et al. 2005), 1.76 kpc (Oh et al. 2010; Mutie et al. 2021), 2.1 kpc (Reid et al. 2009; Shimoikura et al. 2013), 2.2 kpc (Koempe et al. 1989), and 3.5 kpc (Moffat et al. 1979; Saito et al. 2007). In this work, we have adopted a distance of 1.5 kpc, which is obtained from the examination of distances of Global Astrometric Interferometer for Astrophysics (*Gaia*) sources distributed toward the target sites (see Section 3.1 for more details). Previously, Leistra et al. (2006) also used the distance value of 1.5 kpc as an average estimation between the proposed values of Bik et al. (2005) and Koempe et al. (1989). The same distance value is also utilized in the other works (e.g., Carpenter et al. 1993; Devine et al. 2008).

Each of the target sites, T1 and T2 hosts one 6.7 GHz MME with systemic velocities of 2.8 and 1.7 km s⁻¹, respectively (Szymczak et al. 2018). Including the MMEs, several signposts of star formation (i.e., outflow activity, water maser, and young stellar objects (YSOs)) and dense clumps were observed toward both the sites (e.g., Koempe et al. 1989; Davis et al. 1998; Ghosh et al. 2000; Klein et al. 2005; Wu et al. 2010; Shimoikura et al. 2013; Navarete et al. 2015). These sites are spatially found close to an H II region Sh2-247 (hereafter, S247) excited by a massive O9.5 star *LS V +21°27* (Roman-Lopes & Roman-Lopes 2019). The massive star is also known as ALS 8736 or CGO 115 (hereafter, cgo115).

In the direction of the site T1, high-resolution near-infrared (NIR) images from the Integral Field Spectrograph SINFONI on UT4 (Yepun) of the VLT (Vasyunina 2010) and millimeter maps from the Atacama Large Millimeter/submillimeter Array (ALMA) have been examined (e.g., Mutie et al. 2021). Ground-based NIR observations were also made toward T1 (Leistra et al. 2006; Devine et al. 2008), and the age of the NIR cluster toward T1 was reported to be ~2.5 Myr (Devine et al. 2008). Using the NIR spectroscopic study, Vasyunina (2010) obtained a similar age of 1–3 Myr for T1. Previous results also suggested that T1 is younger than T2 (Kurtz et al. 1994; Ghosh et al. 2000). Using the James Clerk Maxwell Telescope (JCMT) 850 μ m dust continuum map, both the sites T1 and T2 were found to be connected by a filamentary feature (see Figure 1 around IRAS 06056+2131 and IRAS 06058+2138 in Klein et al. 2005). Molecular emission were also detected toward this filamentary feature (see Figures 1b and 1c in Shimoikura et al. 2013). However, no study is yet carried out to explore the role of this filamentary feature in star-forming activity in both sites. Carpenter et al. (1995a,b) proposed a triggered star formation scenario for the Gemini OB1 molecular cloud complex, including our selected target sites. Based on the molecular line data, Shimoikura et al. (2013) reported two velocity components around [-3, 5] and [5, 13] km s⁻¹ (see Figure 3b in their paper) and suggested the applicability of cloud-cloud collision (CCC) process in both the sites for explaining the observed star formation activities.

Our selected targets host early phases of MSF and are connected with a filamentary feature as traced in previous studies of dust continuum and molecular line data. However, despite numerous studies on the target sites, no attempt has been made to study embedded filaments and their role in the mass accumulation processes in MSF. In this relation, this paper examines the applicability of the previously proposed CCC scenario and the role of filament in star formation processes. It also attempts to understand the impact of the O-type star cgo115 on the sites T1 and T2. An extensive analysis of the multi-scale and multi-wavelength data sets (see Section 2 for details) has been performed in this relation. Embedded features are studied at small-scales (~0.01 pc) to large-scales (~1 pc) using several continuum images covering NIR to radio wavelengths.

Additionally, molecular line data were employed to examine the kinematics of molecular gas and their spatial distribution.

The paper is arranged as follows. Section 2 describes the details of the data utilized in this work. The observational results are presented in Section 3 and discussed in Section 4. Section 5 summarizes our main findings.

2 DATA SETS

Multi-scale and multi-wavelength data sets were collected from various surveys for our selected target area of 19:58 × 18:33 (centred at $l = 188^\circ 98$, $b = 0^\circ 83$). This work utilized the *Gaia* Early Data Release 3 (EDR3) to estimate the distance of our target source (Gaia Collaboration et al. 2021; Bailer-Jones et al. 2021). A brief description of all other data sets analyzed in this work is presented below.

2.1 NIR data

Deep NIR photometric H and K band magnitudes of point-like sources were obtained from the UKIDSS-Galactic Plane Survey (GPS; Lawrence et al. 2007) and the Two Micron All Sky Survey (2MASS; Skrutskie et al. 2006). We also collected the UKIDSS-GPS K band image for our target area. The UKIDSS-GPS observations (resolution ~0.''8) were made using Wide Field Camera (WFCAM; Casali et al. 2007) mounted on the 3.8 m UK Infra-Red Telescope. We selected only those sources which have photometric errors of 0.1 mag, or less in both the bands. The *Spitzer* IRAC 3.6 and 4.5 μ m images (resolution of ~2.'') and photometric magnitudes of point-like sources were collected from the Warm-*Spitzer* Glimpse 360 (Whitney et al. 2011) survey. The point-like sources with a photometric magnitude error of 0.2 mag, or less in the IRAC 3.6 and 4.5 μ m bands were considered for further analysis. Additionally, we obtained the Hubble Space Telescope (HST) pipeline-calibrated NIR imaging data (resolution ~0.''1–0.''2) in the J (WFC3/F110W), H (WFC3/F160W) wide band filters, and in the [Fe II] (WFC3/F164N) narrow band filter. These images are only available for site T1.

2.2 H₂ narrow band image

Our entire selected target area was covered in the survey of extended H₂ emission (Navarete et al. 2015), which was carried out (with an average seeing of ~0.''7) using the Wide-field InfraRed Camera (WIRCam) mounted on the Canada-France-Hawaii Telescope (CFHT). We used the continuum-subtracted H₂ ($\lambda = 2.122 \mu$ m, $\Delta\lambda = 0.032 \mu$ m) image from this survey (for more details, see Navarete et al. 2015).

2.3 Dust continuum data

We obtained far-infrared (FIR) and sub-millimeter dust continuum images (70–500 μ m) from the *Herschel*¹ Space Observatory data archives, which were collected as a part of *Herschel* Infrared Galactic Plane Survey (Hi-GAL; Molinari et al. 2010). The resolution of

¹ *Herschel* is an ESA space observatory with science instruments provided by European-led Principal Investigator consortia and with important participation from NASA.

the *Herschel* images at 70, 160, 250, 350, and 500 μm are about 6'', 12'', 18'', 25'', and 37'', respectively.

We obtained the *Planck* 353 GHz or 850 μm dust continuum polarization data, comprising of Stokes I, Q, and U maps (resolution $\sim 5'$) for our entire target area (Planck Collaboration et al. 2014). These data were extracted from the *Planck* Public Data Release 3 of Multiple Frequency Cutout Visualization (PR3 Full Mission Map with PCCS2 Catalog). Results derived using the *Planck* polarization data are presented in APPENDIX A.

The high-resolution ALMA 1.3 mm dust continuum images (project id: 2015.1.01454.S, PI: Zhang, Yichen) at two different resolutions (i.e., $0''.18 \times 0''.28$ and $0''.63 \times 1''.23$) were collected toward the site T1 from the ALMA FITS Archive. Note that no ALMA observations were made toward site T2. An analysis of the high-resolution NIR images (from HST and UKIDSS) and the ALMA 1.3 mm dust continuum map can be found in APPENDIX B.

2.4 Molecular CO line data

To explore the gas kinematics, we examined the $^{12}\text{CO}(J=1-0)$; rest frequency (ν_0) ~ 115.27 GHz), $^{13}\text{CO}(J=1-0)$, $\nu_0 \sim 110.20$ GHz) and $\text{C}^{18}\text{O}(J=1-0)$, $\nu_0 \sim 109.78$ GHz) line data toward our selected target area. These molecular line data (beam size $\sim 55''$) were taken as a part of the Milky Way Imaging Scroll Painting (MWISP¹) project. This project is an ongoing northern Galactic plane $^{12}\text{CO}(J=1-0)/^{13}\text{CO}(J=1-0)/\text{C}^{18}\text{O}(J=1-0)$ survey led by the Purple Mountain Observatory (PMO), using the 13.7 m millimeter-wavelength telescope² at Delingha, China. The telescope mapped an area of $0^\circ 5' \times 0^\circ 5'$ using position-switch On-The-Fly (OTF; see Sun et al. 2018) mode with a pointing accuracy better than $5''$. The total bandwidth of 1 GHz, with a frequency interval of 61 kHz, provides 16,384 channels which result in a velocity separation of ~ 0.16 km s⁻¹ for ^{12}CO and ~ 0.17 km s⁻¹ for ^{13}CO and C^{18}O . The achieved rms noise level for ^{12}CO is ~ 0.5 K at the channel width of 0.16 km s⁻¹ and for ^{13}CO and C^{18}O is ~ 0.3 K at the channel width of 0.17 km s⁻¹. These molecular data were reduced using the GILDAS software³ (Pety 2005). More about the telescope and receiver employed in the MWISP project can be found in Su et al. (2019) and references therein.

2.5 Radio continuum data

The 1.4 GHz radio continuum map for our entire target area was collected from the NRAO VLA Sky Survey (NVSS; Condon et al. 1998), and the radio map has the resolution and sensitivity of $\sim 45''$ and ~ 0.45 mJy beam⁻¹, respectively. We also obtained the processed radio continuum map at 8.46 GHz (beam size $\sim 3''.1 \times 2''.3$; rms ~ 36.8 $\mu\text{Jy beam}^{-1}$) from the NRAO Very Large Array Archive Survey (NVAS) toward T1 only.

3 RESULTS

3.1 Physical environment of the target sites T1 and T2

3.1.1 Elongated filament

Figure 1a displays a *Herschel* three-color composite image (red: 250 μm , green: 160 μm , and blue: 70 μm), which is overlaid with the NVSS 1.4 GHz radio continuum emission contours and the position of the previously known massive star, cgo115. The positions of two 6.7 GHz MMEs are also indicated in Figure 1a (see triangles). An elongated filamentary structure is the most prominent feature in the color composite map, which has a dumbbell-like appearance. Each end of the filamentary structure is associated with at least one earlier reported star-forming site, where one 6.7 GHz MME is also traced. The ionized emission outlined through the NVSS 1.4 GHz radio continuum contours shows the spatial extension of the H II region, S247. The massive star, cgo115, seems to be located at the center of the radio continuum emission (see an asterisk in Figure 1a). The NVSS 1.4 GHz radio continuum emission ($1\sigma \sim 0.45$ mJy beam⁻¹) is not detected toward the filamentary structure, including both the star-forming sites. Figure 1b shows the *Herschel* 70 μm image overlaid with the positions of the *Gaia* EDR3 sources (Gaia Collaboration et al. 2021). 170 *Gaia* sources are selected toward areas enclosed by the 70 μm emission contour (see Figure 1b). The photogeometric distances (“rpgeo”) specified in Bailer-Jones et al. (2021) are utilized for the selected *Gaia* EDR3 sources. Figure 1c presents the distance distribution of these *Gaia* sources. Distribution of these *Gaia* sources peaks around 1.5 kpc, which is consistent with the earlier adopted distance for the site T1 (Leistra et al. 2006; Devine et al. 2008). The angular separations of the 6.7 GHz MMEs in T1 and T2 with the position of the massive star, cgo115, are determined to be about $5''.3$ (2.3 pc) and $5''.9$ (2.6 pc), respectively. The angular separation between these two MMEs is about $7''.9$ (3.4 pc). We present the inverted grayscale *Herschel* 250 μm image in Figure 1d. It reveals an elongated filamentary structure (of length ~ 4 pc), hosting T1 and T2 at the opposite edges of the filament.

3.1.2 Hub-filament systems

Apart from the elongated filamentary structure, we notice a HFS toward both the sites AFGL 5180 and AFGL 6366S, where several small scale filaments (i.e., sub-filaments; length ~ 1 pc) appear to direct toward the central regions. To highlight HFSs, zoomed-in views of T1 and T2 are presented using the inverted grayscale FIR map at *Herschel* 250 μm (see insets in Figure 1d). The NVAS 8.46 GHz radio continuum map is available toward site T1. However, site T2 is not covered by the NVAS survey. One can notice that the NVAS survey has better sensitivity than the NVSS survey. In Figure 1d, the position of the radio continuum sources detected in the NVAS 8.46 GHz radio continuum map are presented in the inset on the top-left, indicating the presence of a small cluster of radio sources (or massive stars) toward AFGL 5180.

In order to further examine the embedded structures, we utilized a newly developed algorithm, *getsf* (Men’shchikov 2021) on the *Herschel* 160 μm image (resolution $\sim 12''$). Use of *getsf* disintegrates the astronomical image into its structural components (i.e., sources and filaments) and splits these components from each other and their backgrounds. One can find more details about this algorithm in Men’shchikov (2021). The maximum size of the structural elements (i.e., filaments and sources), the angular resolution of the image, and the source distance are the necessary inputs for the al-

¹ <http://english.dlh.pmo.cas.cn/ic/in/>

² <http://www.radioast.nsd.cnmwisp.php>

³ <http://ascl.net/1305.010> or <http://www.iram.fr/IRAMFR/GILDAS>

gorithm to function. Here, the filamentary skeletons in the *Herschel* 160 μm image are extracted with the maximum source and filament sizes of 20'' and 105'', respectively, and a distance of 1.5 kpc. The outcome of the *gtsf* utility at the scale of 12'' is presented in Figure 2a (see filamentary skeletons in red). Several sub-filaments are identified in the direction of both the sites T1 and T2, which are highlighted on the *Herschel* 160 μm image in Figure 2a. The identified sub-filaments make a junction toward the central part of T1 and T2, which are associated with the 6.7 GHz MMEs (see green triangles in Figure 2a). Therefore, MSF activities are exclusively found at the junctions of several sub-filaments. We have highlighted two distinct structures (i.e., a curved feature F1 and an elongated filament F2) in Figure 2a. The curved feature F1 is observed at the boundary of the H II region traced in the NVSS 1.4 GHz radio continuum emission map. The sites T1 and T2 are seen at opposite edges of filament F2. Hence, the presence of HFSs at opposite edges of an elongated filament is a new picture concerning the target sites.

3.1.3 Feedback of the O-type star

To assess the influence of cgo115 (see a yellow asterisk in Figure 2a) on the curved feature F1 and the filament F2, we have calculated the strength of different pressure components driven by the massive O-type star on these structures. The equations leading to thermal pressure of the ionized gas ($P_{\text{H II}}$), radiation pressure (P_{rad}), and stellar wind ram pressure (P_{wind}) are obtained from Bressert et al. (2012) and given below,

$$P_{\text{H II}} = \mu m_{\text{H}} c_s^2 \left(\sqrt{\frac{3N_{\text{uv}}}{4\pi \alpha_{\text{B}} D_s^3}} \right); \quad (1)$$

$$P_{\text{rad}} = L_{\text{bol}}/4\pi c D_s^2; \quad (2)$$

$$P_{\text{wind}} = \dot{M}_{\text{w}} V_{\text{w}}/4\pi D_s^2. \quad (3)$$

Here, N_{uv} is the number of Lyman continuum photons emitted per second by the ionizing source. The sound speed in the ionized region is $c_s = 11 \text{ km s}^{-1}$ (Bisbas et al. 2009) and the radiative recombination coefficient is $\alpha_{\text{B}} = 2.6 \times 10^{-13} \text{ cm}^3 \text{ s}^{-1}$ (Kwan 1997), assuming the temperature to be around 10^4 K . The mean molecular weight in the ionized gas is $\mu = 0.678$ (Bisbas et al. 2009), and m_{H} indicates the mass of the hydrogen atom. \dot{M}_{w} , V_{w} and L_{bol} are respectively the mass-loss rate through stellar wind, the wind velocity, and the bolometric luminosity of the ionizing source, cgo115. The speed of light (c) is adopted to be $2.9979 \times 10^8 \text{ m s}^{-1}$. D_s is the projected distance between the point of our interest and the massive star. For a O9.5V star, we can adopt $L_{\text{bol}} \approx 66070 L_{\odot}$ (Panagia 1973), $\dot{M}_{\text{w}} \approx 1.58 \times 10^{-9} M_{\odot} \text{ yr}^{-1}$ (Marcolino et al. 2009), $V_{\text{w}} \approx 1500 \text{ km s}^{-1}$ (Martins & Palacios 2017) and $N_{\text{uv}} \approx 1.2 \times 10^{48} \text{ s}^{-1}$ (Panagia 1973).

To calculate the pressure components mentioned above, 16 positions are selected on the structure F1 (see filled hexagons in Figure 2a). The first three positions (i.e., #1, #2, and #3) and the last position (i.e., #16) are mentioned to follow the order of numbering of the positions. For the same purpose, 25 positions are chosen along the filament F2 (see filled crosses in Figure 2a). The pressure components P_{rad} , $P_{\text{H II}}$, and the combined pressure (i.e., $P_{\text{wind}} + P_{\text{rad}} + P_{\text{H II}}$) are displayed in Figures 2b and 2c for positions along F1 and F2, respectively. Hence, we find that along F1, all pressure components fluctuate around their mean values (see horizontal lines in Figure 2b). For F2, the closest position has the highest pressure in all forms, and all pressure components fall on either side as their

distances from the massive star increase. Overall, ionized gas pressure dominates over the other pressure components for our region of interest. The wind pressures present a negligible contribution of about $10^{-16} \text{ dynes cm}^{-2}$ in the total pressure values for both F1 and F2. From Figure 2c, we can infer that the combined pressure values excluding $P_{\text{H II}}$ (i.e., the total of P_{wind} and P_{rad}) along F2 are about $10^{-11} \text{ dynes cm}^{-2}$. It is important to note that the filaments and the massive star are assumed to lie on the same plane as of sky. Thus, our estimated distances represent the lower limit that leads to the upper limit in the estimated pressure values if the projection effect is considered.

3.2 Study of embedded protostars

The detection of YSOs has been adopted as a reliable tool to trace ongoing star formation activity in a given star-forming site. Therefore, the procedure of Gutermuth et al. (2009) is followed to identify the embedded YSOs using the photometric data of point-like objects in the area as shown in Figure 1a. A dereddened color-color diagram (i.e., $[[3.6]-[4.5]]_0$ Vs. $[K-[3.6]]_0$) is presented in Figure 3a, revealing 25 Class I YSOs and 128 Class II YSOs. Additional YSOs are also selected using the NIR color-magnitude diagram (i.e., H–K Vs. K) as displayed in Figure 3b. Following the SQL conditions presented in Lucas et al. (2008), the reliable photometric data in the H and K bands were obtained from the UKIDSS-GPS survey. In general, bright sources are saturated in the UKIDSS-GPS survey. Hence, we also utilized the 2MASS photometric data in the H and K bands. The color-magnitude analysis of a nearby control field provides a color condition of $H - K > 0.63 \text{ mag}$, allowing us to find 109 more YSO candidates. Altogether, 208 YSO candidates are selected after considering the common sources extracted from these two schemes. In Figure 3c, the positions of these selected YSOs are overlaid on the *Herschel* 70 μm image.

The nearest neighbor (NN) surface density analysis is a useful tool to assess groups/clusters of the YSOs in star-forming regions (see, e.g., Casertano & Hut 1985; Bressert et al. 2010; Dewangan et al. 2017a; Bhadari et al. 2020). We have also adopted this technique to compute the surface density map of YSOs in our target area. The target area, as shown in Figure 1a is divided into 100×100 grid lines, corresponding to the separations of 11''7 and 11''1 along the Galactic longitude and latitude, respectively. Considering $d = 1.5 \text{ kpc}$ and $\text{NN} = 5$, the surface density map of YSOs is produced. In Figure 3c, *Herschel* 160 μm image is overplotted with YSOs surface density contours at the levels of 15 – 300 YSOs pc^{-2} . Clusters of YSOs CL1 and CL2 are seen toward the sites T1 and T2, respectively (see yellow dotted circles in Figure 3c). Noticeable YSOs are also traced toward the central part of the elongated filament. Hence, our analysis reveals the ongoing star formation activities toward the entire filament F2, and the clusters of YSOs are mainly found toward the edges of the filament.

3.3 Spitzer ratio map and continuum-subtracted H₂ emission

The *Spitzer* ratio map (i.e., $4.5 \mu\text{m}/3.6 \mu\text{m}$) and the narrow band H₂ ($\nu = 1 - 0 \text{ S}(1)$, $2.12 \mu\text{m}$) emission are very useful to trace the energetic feedback of massive stars and/or star formation activities in a given molecular cloud (see Povich et al. 2007; Dewangan et al. 2017a; Pandey et al. 2020). A detailed description of the H₂ emission in massive star-forming sites M 17 UC1 – IRS5 can be found in Chen et al. (2015). In this context, Figure 4a presents the *Spitzer* ratio map for our target area. Bright regions in the ratio map present

an excess of $4.5\ \mu\text{m}$ emission over $3.6\ \mu\text{m}$ emission, while the exact inverse condition is true for the dark regions. The continuum-subtracted H_2 ($\nu = 1 - 0$ S(1)) map is produced using a similar approach discussed in Navarete et al. (2015). Figure 4b presents the continuum-subtracted H_2 ($\nu = 1 - 0$ S(1)) map for a region highlighted with a magenta rectangle in Figure 4a.

The *Spitzer* $4.5\ \mu\text{m}$ band includes contributions from H_2 ($\nu = 0 - 0$ S(9), $4.693\ \mu\text{m}$) and $\text{H I Br-}\alpha$ recombination line emission ($4.05\ \mu\text{m}$). On the other side, *Spitzer* $3.6\ \mu\text{m}$ band covers far-ultraviolet (FUV) heated polycyclic aromatic hydrocarbon (PAH) $3.3\ \mu\text{m}$ emission from C–H vibrational stretching mode (Allamandola et al. 1989; Draine 2003; Tielens 2008) and H_2 ($\nu = 1 - 0$ O(5), $3.234\ \mu\text{m}$). Due to an excess of $4.5\ \mu\text{m}$ over $3.6\ \mu\text{m}$ emission in the ratio map, bright regions are found toward the entire elongated filament feature (including the sites T1 and T2; see Figure 4a), where the extended radio continuum emission is absent. In Figure 4b, the H_2 ($\nu = 1 - 0$ S(1)) emission is also seen toward the filament. Hence, Figures 4a and 4b support the presence of outflow activities toward the entire filament (including T1 and T2), indicating the ongoing star formation activities (see also clusters of YSOs in Section 3.2). Dark features in the ratio map are traced at the periphery of the H II region, S247 (see also the curved feature F1), showing an excess of PAH-dominated $3.3\ \mu\text{m}$ emission. A similar characteristic is also traced around the Galactic H II region S305 using the *Spitzer* ratio map (e.g., Dewangan et al. 2020a; Bhadari et al. 2021). Therefore, the dark regions in the ratio map may display the photo-dissociation regions (PDRs), suggesting the influence of the massive star on its surrounding.

3.4 Herschel column density and dust temperature maps

The multi-wavelength *Herschel* images allow the computation of the column density ($N(\text{H}_2)$) and the dust temperature (T_d) maps for a region indicated by a green rectangle in Figure 4a. A pixel-by-pixel spectral energy distribution (SED) fitting with a modified blackbody spectra provides the desired physical parameters (i.e., $N(\text{H}_2)$ and T_d) at each pixel. Despite the availability of the *Herschel* $70\ \mu\text{m}$ image, this has been excluded from the SED fitting because it generally contains contamination from ultraviolet (UV) heated dust of much higher temperatures. We utilized the tool *hires* (Men'shchikov 2021) to produce the high-resolution column density and dust temperature maps. The basic concept behind these high-resolution maps is the addition of higher-resolution information to the lower-resolution images as differential terms (see Equation A.1 in Palmeirim et al. 2013). More details can be found in Men'shchikov (2021). The use of the *Herschel* images (i.e., $70\text{--}500\ \mu\text{m}$) in *hires* provides up to the best resolution available among the input images (i.e., $\sim 6''$ for *Herschel* $70\ \mu\text{m}$ image). However, the resulting column density and dust temperature maps of $6''$ resolution are noisy, which may be due to insignificant features present in the *Herschel* $70\ \mu\text{m}$ image. Hence, we have utilized the column density and dust temperature maps of resolution $\sim 12''$ in this work, which are presented in Figures 4c and 4d, respectively. In the direction of the HFSs (see arrows toward T1 and T2 in Figure 4c), the central hubs or junctions of the sub-filaments hosting the $6.7\ \text{GHz}$ MMEs are found with higher column densities ($N(\text{H}_2) \sim 10^{23}\ \text{cm}^{-2}$). The central hubs are traced with higher dust temperatures of $22\text{--}26\ \text{K}$ (see Figure 4d). Figure 4e displays a two-color composite image using the column density map (in red) and the dust temperature map (in cyan). In Figure 4e, the filament F2 and the curved feature F1 are clearly distinguished in the *Herschel* temperature map (see also Figure 4d). The curved feature F1 shows a relatively higher dust temperature than the fila-

ment F2 except for its edges. In other words, the elongated filament F2 has a higher column density and lower dust temperature, but the curved structure F1 has a higher dust temperature and lower column density.

3.4.1 Study of Herschel clumps and their physical parameters

To study the fragmentation (or to detect clumps) in the column density map, we employed the *clumpfind* algorithm (see for details Williams et al. 1994). A total of 16 clumps are identified in the column density map, and their boundaries and IDs are shown in Figure 4f. The mass (M_{clump}) of each clump can be estimated using,

$$M_{\text{clump}} = \mu_{\text{H}_2} m_{\text{H}} \text{Area}_{\text{pixel}} \Sigma N(\text{H}_2) \quad (4)$$

Here, m_{H} is the mass of a hydrogen atom, μ_{H_2} is the mean molecular weight, $\text{Area}_{\text{pixel}}$ is the area subtended by one pixel, and $\Sigma N(\text{H}_2)$ is the total column density. The value of μ_{H_2} is adopted to be 2.8. Various physical parameters (including mass) of these 16 clumps are listed in Table 1. The clump masses range from 27 to $498 M_{\odot}$. Massive clumps (IDs: #1 and #2) are located toward the massive star-forming regions T1 and T2, respectively. Additionally, several fragments/clumps (IDs: #3, #4, #5, #6, #9, and #10; see also Table 1) are also seen along their connecting filament F2 (see Figure 4f).

3.4.2 The physical parameters of the sub-filaments

In order to understand the variation of the column density and dust temperature along the sub-filaments toward AFGL 5180 and AFGL 6366S, we have chosen several circular regions of radius $7''$ along the sub-filaments. In Figure 5a, the *getsf* identified sub-filaments toward AFGL 5180 and AFGL 6366S are only shown with gray skeletons on the *Herschel* column density map. The selected circular regions along the sub-filaments are also overplotted. The average column density and dust temperature values for these circular regions are plotted as a function of distances along the sub-filaments from corresponding hubs in Figures 5b and 5c, respectively. For both AFGL 5180 and AFGL 6366S, lengths of the associated filaments are within $1\text{--}2\ \text{pc}$. All the sub-filaments toward AFGL 6366S are traced with higher dust temperatures ($\sim 16\text{--}23\ \text{K}$) and lower column density ($\sim 5 \times 10^{21}\text{--}2 \times 10^{22}\ \text{cm}^{-2}$) compared to sub-filaments of AFGL 5180 ($T_d \sim 13\text{--}19\ \text{K}$ and $N(\text{H}_2) \sim 5 \times 10^{21}\text{--}2 \times 10^{22}\ \text{cm}^{-2}$). For sub-filaments, the average dust temperature and column density values peak at their junctions/hubs and then decrease along their lengths as moving away from the hubs. The trend of increasing column density along the filaments toward the hub has also been reported in one of the most well-known HFSs, Mon R2 (see Figures 2 and 3 in Kumar et al. 2022).

3.5 Probing the distribution of molecular gas

In this section, we have examined the CO line data to study the gas distribution in both the spatial and velocity space. The details of the molecular data are given in Section 2.

3.5.1 Distribution and kinematics of molecular gas

In this section, we have presented the integrated intensity (moment-0) maps, the intensity-weighted velocity (moment-1) maps, and the intensity-weighted full width at half maximum (FWHM) linewidth map of the ^{12}CO , ^{13}CO , and C^{18}O emission in the direction of our target sites for an area, shown via a magenta rectangle in Figure 3c.

Table 1. List of the physical parameters of the detected *Herschel* clumps. R_{clump} is the effective radius and $[N(\text{H}_2)]_{\text{peak}}$ presents the peak column density. $[T_{\text{d}}]_{\text{peak}}$ and $[T_{\text{d}}]_{\text{mean}}$ stand for the peak and mean dust temperature, respectively.

ID	l (degree)	b (degree)	R_{clump} (pc)	M_{clump} (M_{\odot})	$[N(\text{H}_2)]_{\text{peak}}$ ($\times 10^{22} \text{ cm}^{-2}$)	$[T_{\text{d}}]_{\text{peak}}$ (K)	$[T_{\text{d}}]_{\text{mean}}$ (K)
1	188.951	0.882	0.39	498	36.48	26	19
2	189.030	0.781	0.35	274	22.30	36	21
3	189.032	0.808	0.32	261	12.69	22	18
4	189.032	0.790	0.25	128	7.10	27	20
5	189.014	0.826	0.24	91	3.72	17	15
6	189.007	0.839	0.25	74	3.66	17	15
7	188.975	0.911	0.19	46	3.21	15	14
8	188.966	0.922	0.37	156	3.19	15	13
9	188.991	0.871	0.30	97	3.03	16	15
10	188.992	0.859	0.21	51	2.70	16	15
11	188.977	0.904	0.26	70	2.63	16	15
12	188.953	0.903	0.30	105	2.55	24	17
13	188.910	0.897	0.32	101	2.53	17	14
14	188.974	0.918	0.30	106	2.43	15	13
15	188.958	0.889	0.22	54	2.43	26	20
16	188.902	0.762	0.16	27	1.83	14	14

In all the moment maps, the NVSS radio continuum contour (at 3σ) tracing the boundary of the ionized region, the positions of the 6.7 GHz MMEs, and the location of the massive O-type star are shown. In general, the C^{18}O emission is optically thin compared to the ^{12}CO and ^{13}CO emission, and traces the denser regions of the molecular cloud. All the moment-0 maps show almost identical morphology and support the existence of an elongated molecular cloud hosting T1 and T2 at its opposite edges. Both T1 and T2 show intense $^{12}\text{CO}/^{13}\text{CO}/\text{C}^{18}\text{O}$ molecular gas emission compared to their filamentary connection. Figures 6b, 6e, and 6h present the moment-1 maps of ^{12}CO , ^{13}CO , and C^{18}O , respectively. Noticeable velocity variations (of about 1-2 km s^{-1}) are observed between star-forming sites (i.e., T1 and T2) and their connecting filament. The filaments detected from the dust continuum emission are overplotted on the moment-1 map for the ^{13}CO and C^{18}O emission (see Figures 6e and 6h, respectively). The filamentary connection between two intense molecular emissions (at T1 and T2) is mainly detected in the velocity range [1.3, 2.7] km s^{-1} in Figures 6e and 6h. Despite the coarse beam size of the molecular line data compared to *Herschel* 160 μm dust continuum image used to trace the filaments, the moment-0 maps show an elongated morphology spatially coexisting with filament F2. However, sub-filaments are not observed in the moment-0 maps. In Figures 6c, 6f, and 6i, we display the linewidth maps of ^{12}CO , ^{13}CO , and C^{18}O data, respectively. Overall, ^{12}CO linewidth map shows the largest values, while C^{18}O presents the least in the same. But in all the lines, relatively higher line width values are found toward the edges of the filament (i.e., toward T1 and T2) compared to their connecting filament.

We have highlighted some circular regions of radius $30''$ along the filament F2 in Figure 4e, and various physical parameters along the filament are extracted. The average column density and dust temperature values for the circular regions are presented in Figures 7a and 7b, respectively. These values are estimated using the *Herschel* column density and dust temperature maps, which are shown in Figures 4c and 4d, respectively. Higher values of column density and dust temperature are observed toward T1 and T2. Using the ^{13}CO and C^{18}O molecular line data, we have also computed average velocity, thermal sound speed ($a_s = (kT_{\text{kin}}/\mu m_{\text{H}})^{1/2}$), non-thermal velocity dispersion (σ_{NT}), and the ratio of thermal to non-thermal

pressure ($P_{\text{TNT}} = a_s^2/\sigma_{\text{NT}}^2$) for the same circular regions. Here, T_{kin} is the kinetic gas temperature. For the calculations of different physical parameters for each circular region, we have assumed T_{kin} to be equal to the average dust temperatures. The mean molecular weight per particle μ is adopted to be 2.37. The thermal and non-thermal velocity dispersion (i.e., σ_{T} and σ_{NT} , respectively) for a molecular line can be derived using,

$$\sigma_{\text{T}} = (kT_{\text{kin}}/\chi m_{\text{H}})^{1/2}, \quad (5)$$

$$\sigma_{\text{NT}} = \sqrt{\frac{\Delta V^2}{8 \ln 2} - \frac{kT_{\text{kin}}}{\chi m_{\text{H}}}} = \sqrt{\frac{\Delta V^2}{8 \ln 2} - \sigma_{\text{T}}^2}, \quad (6)$$

where, χ is the mass of the molecules in terms of hydrogen atomic mass and ΔV is the measured linewidth for the molecular line data. Therefore, $\chi \sim 29$ and ~ 30 for ^{13}CO and C^{18}O , respectively. From the average velocity and non-thermal velocity dispersion profile for ^{13}CO and C^{18}O as shown in Figures 7c and 7d, respectively, it can be observed that T1 and T2 correspond to higher velocity and non-thermal velocity dispersion. Additionally, T1 shows higher velocity than T2, and an oscillation in velocity profile is evident in both ^{13}CO and C^{18}O data. The profile for Mach number (i. e., $M = \frac{\sigma_{\text{NT}}}{a_s}$) and thermal to non-thermal pressure ratio are shown in Figures 7e and 7f, respectively. From the Mach number profile, derived using C^{18}O , we can find that the star-forming sites T1 and T2 are supersonic (with $M > 3$). However, Mach number profile for the C^{18}O data drops down to ~ 2 toward the filamentary connection between T1 and T2 (see Figure 7e). Mach number profile extracted using the ^{13}CO line data reveals the supersonic nature of the filament (i.e., $M > 3$; see Figure 7e). The filamentary structure F2 is traced with lower non-thermal velocity dispersion, leading to higher thermal to non-thermal ratios compared to T1 and T2 in C^{18}O data. In Figure 7f, the values of P_{TNT} are different in the ^{13}CO and C^{18}O emissions. Because the C^{18}O data is optically thin compared to the ^{13}CO emission. Therefore the C^{18}O emission is less affected by the opacity broadening (Phillips et al. 1979; Hacar et al. 2016; Yang et al. 2022).

3.5.2 Identification of the molecular cloud components

In order to probe the complete picture of the molecular gas distribution toward our target sites, we analyzed ^{13}CO data for an extended area of $\sim 1^\circ \times 1^\circ$ (or $\sim 26 \text{ pc} \times 26 \text{ pc}$). The extended moment-0 map of ^{13}CO data is shown in Figure 8a for a velocity integration range of $[-5.1, 15.1] \text{ km s}^{-1}$. The moment-0 map presents a complex morphology of the molecular cloud. Figure 8b presents *Herschel*'s view of the extended region at $250 \mu\text{m}$. The *Herschel* dust continuum data shows the elongated filamentary structure embedded in the molecular cloud, hosting the 6.7 GHz MMEs at its opposite edges. In Figure 8c, the moment-1 map for the ^{13}CO data infers intensity-weighted velocity distribution. Two extreme velocity ranges can be observed in the moment-1 map based on the colorbar in colors blue and red. The average intensity profile extracted for the rectangular region (in black) presented in Figure 8c is shown in the inset. It shows two velocity components with their peaks at the velocities $\sim 2.7 \text{ km s}^{-1}$ and $\sim 6.4 \text{ km s}^{-1}$ for the blue-shifted and red-shifted components, respectively (see the blue and red vertical lines). The blue-shifted and red-shifted components are separated by a velocity of about 3.7 km s^{-1} . To determine the velocity ranges for the cloud components, the Galactic latitude–velocity ($b-v$) diagram is presented in Figure 8d. The $b-v$ diagram is presented for the area shown by white dotted rectangle in Figure 8a. This diagram reveals a clear signature of the presence of two cloud components; the blue-shifted (hereafter, blue) component: $[-3.1, 4.8] \text{ km s}^{-1}$ and the red-shifted (hereafter, red) component: $[5.8, 12.9] \text{ km s}^{-1}$. Both the cloud components are found to be connected with weak molecular emission in an intermediate velocity range $[4.8, 5.8] \text{ km s}^{-1}$, which is shown with two yellow dashed lines in Figure 8d.

3.5.3 Spatial distribution of molecular cloud components

The moment-0 maps for the blue and the red cloud components are shown in colors cyan and red, respectively, in Figure 9a. The moment-0 map of the red component is only displayed within the boundaries of the yellow dashed rectangle. A complementary spatial distribution of the cloud components can be observed in Figure 9a. However, a more convincing picture of their complementarity is achieved by shifting the red cloud component toward the south-west direction by about 2.3 pc , presented in Figure 9b. The initial (i.e., before displacement) and the final (i.e., after displacement) positions of the red cloud component are marked by a dashed and a solid yellow rectangle, respectively. The massive star-forming sites (i.e., the position of the 6.7 GHz MMEs indicated with the triangles) are spatially found toward the junction of two cloud components (see in Figure 9b).

Section 4 presents the implication of these observed results.

4 DISCUSSION

Using the *Herschel* image at $160 \mu\text{m}$, the outcome of the *getsf* utility shows two interesting structures in our target area: the curved feature F1 and the elongated filament F2. The curved feature F1 is associated with the PAH emission at $3.3 \mu\text{m}$ and is located at the boundary of the H II region, S247. The edges of filament F2 are located within sites T1 and T2, both of which also host HFS. Signatures of outflow activities and YSOs are found toward the entire filament F2. Interestingly, the groups of YSOs and the 6.7 GHz MMEs are mainly concentrated at the opposite edges of F2. Using

the ^{12}CO , ^{13}CO , and C^{18}O emission, both the HFSs are depicted with supersonic and non-thermal gas motions having higher Mach number and lower thermal to non-thermal pressure ratio (see Figure 7). The velocity dispersion is found to be higher at the filament's edges compared to the central region, suggesting intense star formation activities at the edges. Earlier studies proposed the CCC and triggered star formation scenarios in our selected target area. Based on our observational findings, we have carefully assessed these scenarios and the role of filaments in the below sections.

4.1 Impact of the massive star on its environment

In general, Lyman continuum photons of a massive star ionize the surrounding medium and create an H II region. This H II region expands supersonically in the surrounding neutral gas medium, which drives a shock. Based on this property, in the literature, the ‘‘collect and collapse’’ (C&C; Elmegreen & Lada 1977) and the radiatively driven implosion (RDI; Bertoldi 1989) scenarios have been proposed to explain triggered star formation. In the RDI model, star formation activities are produced by the compression of the pre-existing dense clumps by the shock wave. In the C&C scenario, the shock continues to sweep up cool neutral gas to form a massive and dense shell around the H II region (Deharveng et al. 2005; Dale et al. 2007). Over time this shell of collected gas becomes gravitationally unstable, and collapses to form new stars.

In our target area, a cavity in the molecular gas distribution is seen in all the moment-0 maps (see the cyan contour in Figures 8a, 8d, and 8g). This cavity in molecular gas shows a footprint of the interaction between the molecular gas and ionizing photons. The curved feature F1, which is deprived of molecular emission, is located close to the massive O-type star (i.e., cgo115). In contrast, filament F2 traced in the molecular and dust continuum maps appears further away from F1 and cgo115. Considering an excess of PAH $3.3 \mu\text{m}$ emission in the *Spitzer* $3.6 \mu\text{m}$ band, the impact of the O-type star on the curve feature F1 is likely. All the derived pressure components (i.e., P_{wind} , P_{rad} , and $P_{\text{H II}}$) have consistent values along F1. Among them, $P_{\text{H II}}$ is the most dominating while P_{wind} contributes the least. The combined pressure value along F1 is about $10^{-10} \text{ dynes cm}^{-2}$, well above the typical molecular gas pressure ($\sim 10^{-11} \text{ dynes cm}^{-2}$; see Table 7.3 in Dyson & Williams 1997). Therefore, the feedback from cgo115 seems sufficient to form the feature F1 and may be responsible for its curved appearance. Similar pressure analysis along the filament F2 (see Figure 2c) shows that every pressure component falls as we move away from the central point. Interestingly, as the H II region is not directly associated with F2 (see the cyan contour in Figure 2a), therefore, we can exclude $P_{\text{H II}}$ while computing combined pressure. Now, the total of wind and radiation pressure along F2 peaks at around $1.5 \times 10^{-11} \text{ dynes cm}^{-2}$; hence it can be balanced by the molecular gas pressure. Including $P_{\text{H II}}$, we find the peak of the combined pressure around $10^{-10} \text{ dynes cm}^{-2}$. Therefore, cgo115 has the potential to impact F2 in the future. But the current pressure values along F2 and its linear morphology do not allow us to connect its origin due to the feedback of the massive star, cgo115. The combined pressure values of cgo115 at the massive star-forming sites T1 and T2 (residing at the edges of F2) are also not significant to affect the star-formation activity. Therefore, we do not find triggered star formation scenarios feasible in these star-forming regions. This proposal agrees with the previously reported work of Vasyunina (2010). By analyzing NIR spectroscopic data of the AFGL 5180 cluster, Vasyunina (2010) found that the more evolved stars are located further away from the H II region, whereas the younger sources that are driving outflows

are situated closer to the H II region. This signature is opposite to the prediction of the triggered star formation scenarios (Dale et al. 2007, 2015).

4.2 Role of filaments toward our target sites

A small cluster of the radio continuum sources toward the site T1 and the 6.7 GHz MMEs toward the sites T1 and T2 together support the ongoing MSF activities in both the HFSs. Junctions of the sub-filaments (i.e., hubs) show higher column density and dust temperature toward T1 and T2. We suggest that the mass accumulation through sub-filaments may be the possible scenario for the MSF activity toward T1 and T2 (e.g., Myers 2009; Tan et al. 2014; Tigé et al. 2017; Motte et al. 2018; Treviño-Morales et al. 2019; Rosen et al. 2020; Dewangan et al. 2022). Concerning the observed hub-filament configurations, the proposed paradigm of MSF by Motte et al. (2018) starts with the formation of density-enhanced hubs at the junctions of several filaments. These hubs host massive dense cores (MDCs), which harbor low-mass prestellar cores during their starless phase. Over time these MDCs become protostellar in a time scale of around 3×10^5 yrs. They host infra-red (IR) quite low-mass stellar embryos ($< 8 M_{\odot}$) at this stage. They grow into IR bright high-mass ($> 8 M_{\odot}$) protostars via gravitationally driven inflows, and then these sources become massive stars that excite H II regions (see more details in Motte et al. 2018). This scenario supports the picture of a mass accumulation from the large-scale to the dense core-scale through filaments (Tigé et al. 2017; Motte et al. 2018; Treviño-Morales et al. 2019). Earlier, Minier et al. (2001) suggested that the 6.7 GHz MMEs most likely trace the massive protostellar phase in the early stages of MSF. Concerning the evolutionary paradigm of MSF, Motte et al. (2018) proposed that the massive protostar is equivalent to the “high-mass protostellar phase.”

A recent study by Kumar et al. (2020) aimed to identify HFSs in the Milky Way. They analyzed approximately 35000 Hi-GAL clumps located within the Galactic longitude range of $68^{\circ} \geq l \geq -72^{\circ}$ and a Galactic latitude range of $|b| \leq 1^{\circ}$ from the study of Elia et al. (2017). To identify the filamentary skeletons associated with the clumps, they used the DisPerSE algorithm (Sousbie 2011) on $10' \times 10'$ cut-outs of Herschel 250 μm images. The study found around 3700 candidate HFSs, constituting approximately 11% of the total clumps analyzed. The filaments forming the HFSs had a mean length of about 10-20 pc. The study also found that all the clumps with luminosity greater than 10^4 and $10^5 L_{\odot}$, at distances within 2 kpc and 5 kpc, respectively, were located in the hubs of HFSs. Typically, the hubs were found to have 3-7 skeletons joining at the junction. In this context, the identification of HFSs in AFGL 5180, and AFGL 6366S provides further insights into the nature and properties of these structures. The Hi-GAL clumps toward AFGL 5180 and AFGL 6366S have luminosities of $\sim 10^3$ and $\sim 10^4 L_{\odot}$ (Elia et al. 2021), respectively. Both the clumps host 6.7 GHz MMEs as the signpost of massive star-forming activity, and they are associated with at least 4 filaments detected based on *Herschel* 160 μm image. From the diameter of the circular regions (i.e., $14''$) used to determine the average properties along the filaments, the widths of the detected filaments can be roughly estimated to be ~ 0.1 pc, which is consistent with the typical width of *Herschel* filaments (André et al. 2022). The column density and dust temperature values increase along the filaments in the direction to the hubs. The flow of dust and gas through the filaments amplifies the column density of the hub, suiting it for MSF (Myers 2009; Kumar et al. 2020; Dewangan et al. 2022). The length of the filaments participating in the formation of HFSs toward our target sites is nearly 1–2 pc. Therefore, for nearby

regions ($d \lesssim 2$ kpc), one can expect more HFSs with parsec-scale filaments. This proposal also agrees with the filament selection criteria of Kumar et al. (2020) because the length scale associated with the image’s resolution increases with distance. It is also noticeable that, though the Hi-GAL clump at AFGL 5180 has a luminosity of $\sim 10^3 L_{\odot}$, it is an observed massive star-forming site. Therefore, we can also expect more such sources in the analysis of 360° *Herschel* data. Hence, a similar analysis like Kumar et al. (2020) for the Hi-GAL 360° clumps (Elia et al. 2021) with *Herschel* 160/250 μm images can reveal more details about HFSs.

In star formation study, it is evident that molecular clouds often create filamentary structures, which further fragment into dense cores (e.g., André et al. 2010). Our molecular gas study shows a similar filamentary structure further fragmented in dense cores toward its edges. Recently, Clarke et al. (2020) found that the filaments are more prone to fragment into sub-filaments, which are responsible for the formation of hubs via their merging event, and the cores formed at the filament’s edges are more massive than the interior ones. The coarse beam sizes of the molecular line data are one of the key obstacles in studying such aspects. Therefore, such a study is beyond the scope of this work.

A connection between CCC and the origin of filaments and HFSs was found in Smoothed particle hydrodynamics simulation by Balfour et al. (2015) for head-on colliding clouds. According to Balfour et al. (2015), CCC produces a shock-compressed layer, which fragments into the filaments. For lower collision velocity, filaments predominantly appear radial, while for higher collision velocity formation of filaments looks like a spider’s web. Recent works of Fukui et al. (2019), Tokuda et al. (2019), and Maity et al. (2022) presented the observational connections between CCC and the formation of HFS.

4.3 Cloud-cloud collision scenario

The CCC scenario is an effective triggering mechanism of MSF. Molecular clouds often collide due to intra-molecular cloud velocity dispersion (typically with a collision rate of 1 in every 100 years; Tasker & Tan 2009; Dobbs et al. 2015). If the collision speed is supersonic, it creates a shock-compressed interface with an increased effective sound speed (Habe & Ohta 1992; Ananthpindika 2010; Fukui et al. 2014, 2018b). It provides a higher mass accretion rate leading to higher ram pressure to overcome the radiation pressure. The observational signatures of CCC are the bridge feature in the position-velocity (PV) space and the complementary spatial distribution of the cloud components (e.g., Torii et al. 2011, 2015, 2017, 2021; Fukui et al. 2014, 2015, 2018a,b, 2021a; Dewangan 2017; Nishimura et al. 2017; Hayashi et al. 2018; Sano et al. 2017, 2018; Fujita et al. 2021). The bridge feature is a low-intensity connection between two cloud components in the PV space (e.g., Haworth et al. 2015; Torii et al. 2017; Dewangan & Ojha 2017; Priestley & Whitworth 2021). The collision of clouds results in a cavity in the larger cloud due to the conservation of linear momentum, referred to as the complementary distribution.

Based on the analysis of $^{12}\text{CO}(J = 2-1)$ data (beam size $\sim 2.7''$), earlier Shimoikura et al. (2013) proposed CCC as a possible triggering mechanism in our target sites (see Figures 3b and 4 in their paper). They reported two clouds at the velocities of $[-3, 5]$ and $[5, 13] \text{ km s}^{-1}$. In Section 3.5.2, we have also found the existence of two clouds (around $[-3.1, 4.8]$ and $[5.8, 12.9] \text{ km s}^{-1}$), which are connected by a bridge feature in velocity space. Additionally, we have investigated a spatial fit of “key/intensity-enhancement” and “cavity/keyhole/intensity-depression” features (i.e., complementary

distribution) of two clouds, which is further strengthened after a spatial shift of about 2.3 pc in the red cloud component. Previously, Fukui et al. (2018b) detected an identical signature of CCC (i.e., complementary distribution with a spatial shift) toward M43 for the formation of massive stars in the Orion Nebula Cluster (see Figures 10 and 11 in Fukui et al. 2018b). The PV diagrams depend upon the angle (α) between the axis of collision and the line of observation, which is thoroughly explained in Fukui et al. (2018b). Earlier, Maity et al. (2022) assumed $\alpha \sim 10^\circ$ based on minute skewness of the “V” like feature in PV diagram for the CCC scenario in the W31 complex. It is important to note that the PV diagram also depends upon the spatial morphology of the molecular cloud components. Therefore, the detection of two cloud components toward our target sites in the PV diagram ensures that the angle (α) is below 90° (Fukui et al. 2018b, 2021b). On the other hand, the requirement of spatial shift for the complementary distribution hints the angle α to be greater than 0° (Fukui et al. 2018b, 2021b). Therefore, it is logical to use the α value in between 30° to 60° for the estimation of the collision time scale. If the observed velocity difference between the colliding clouds is V_{obs} , then along the collision axis it would be, $V_{\text{loc}} = \frac{V_{\text{obs}}}{\cos \alpha}$. Similarly, spatial shift along the collision axis would be, $l_{\text{loc}} = \frac{l_{\text{obs}}}{\sin \alpha}$, for the observed spatial shift of l_{obs} in the sky plane. Finally, the collision time scale can be obtained by, $t_{\text{collision}} = \frac{l_{\text{loc}}}{V_{\text{loc}}}$. In case of present study, the observed velocity and spatial shift are $V_{\text{obs}} = 3.7 \text{ km s}^{-1}$ and $l_{\text{obs}} = 2.3 \text{ pc}$, respectively. Thus for various values of α , i.e., $\alpha = 30^\circ, 45^\circ$, and 60° , $t_{\text{collision}}$ is found to be 1.05, 0.60, and 0.35 Myr, respectively. Hence, a collision between molecular clouds about 1 Myr ago initiated the massive star-forming activity toward our target sites. However, it is interesting to note that previous studies determined the age of the NIR cluster to be ~ 2.5 Myr (Devine et al. 2008; Vasyunina 2010). This infers that the colliding clouds were active in low-mass star formation well before the collision took place. As earlier mentioned, CCC is emerging as a potential mechanism of HFS formation in both theoretical and observational studies (Balfour et al. 2015; Fukui et al. 2019; Tokuda et al. 2019; Maity et al. 2022). It is also interesting to note that our target sites host two HFSs at the edges of a primary filament F2; to date, only a few such systems are reported in the literature (e.g., the filamentary clouds G45.1+0.3 (Bhadari et al. 2022), IC 5146 dark Streamer (Wang et al. 2019; Dewangan et al. 2023), and NGC 6334 (Zernickel et al. 2013; Arzoumanian et al. 2021)). These results thus open a new window for discussion for the formation of HFSs at the edges of a filament.

4.4 End-dominated collapse scenario

Wang et al. (2019) proposed a scenario for the formation of HFSs at the edges of a main filament in their study of IC 5146 dark Streamer, which includes the role of the magnetic field in addition to the gravitational instability of an isolated filament. Once a primary filament becomes supercritical (both thermally and magnetically), it collapses along its major axis because of gravity. Due to the effect of end-dominated collapse (EDC) or edge collapse, massive fragments are exclusively found at the edges of the filament. According to Bastien (1983); Pon et al. (2012); Clarke & Whitworth (2015), the differential gravitational acceleration along the longer axis of an isolated filament drives EDC depending upon the aspect ratio of the filament. During this process, the ram pressure exerted by gas motion is sufficient to pinch the magnetic field lines and forms the U-shaped magnetic field (or bending effect; see more details in Gómez et al. 2018; Wang et al. 2019) at the filament’s edges. A recent study by

Wang et al. (2019) and Chung et al. (2022) suggested that the EDC filament IC 5146 prefers to show the bending effect at its edges. Using *Planck* polarization data, Dewangan et al. (2023) verified this bending effect in nearby ($d \lesssim 2 \text{ kpc}$) EDC filaments (i.e., NGC 6334; Zernickel et al. (2013), S242; Dewangan et al. (2019); Yuan et al. (2020), IC 5146; Wang et al. (2019); Chung et al. (2022), and Mon R1; Bhadari et al. (2020)). Finally, the massive components accumulated at the edges of the primary filament fragments further along the curved magnetic fields to form HFSs (see Figure 13 in Wang et al. 2019).

In literature, apart from IC 5146, the filamentary clouds G45.1+0.3 (Bhadari et al. 2022) and NGC 6334 (Zernickel et al. 2013; Arzoumanian et al. 2021) serve as the sites where the EDC and HFSs are simultaneously investigated. Although signatures of MSF, massive dust clumps, higher column densities, and clusters of YSOs are mainly depicted toward both the edges of the filament F2, our analysis of *Planck* polarization data (see the details in Appendix A) does not clearly show the bending effect (see Figure A1a) to draw a conclusive statement on the EDC process. New high-resolution polarization data toward our target area can shed more light on the bending effect toward both edges of F2. In addition, we conducted a core-scale study of the AFGL 5180 region to investigate the outflow activity and physical association between the 6.7 GHz MME and NVAS 8.46 GHz radio continuum emission with embedded dust cores. To accomplish this, we utilized high-resolution NIR images and ALMA 1.3 mm dust continuum emission. The results of our study are presented in Appendix B.

Altogether our observational results suggest that CCC had initiated the star-forming activity around 1 Myr ago toward the massive star-forming sites AFGL 5180 and AFGL 6366S. Also, the observed HFSs at both edges of the filament can be the consequence of the CCC scenario. However, we suggest that the magnetic field and differential gravitational acceleration can also shape the observed morphology of the target sites. In the context of mass accumulation toward our target sites, we suspect that the clumps in the central hub accumulate materials through filamentary accretion. Then it is also possible that individual cores may grow in mass, sharing the common source of gas and dust within the clump. In other words, the final masses of the stars inside the clump are determined not only by the small clump- or core-scale mass accretion but also by the larger scale, filamentary mass accretion.

5 SUMMARY AND CONCLUSIONS

To unveil star formation processes, we have performed a multi-scale and multi-wavelength study of two massive star-forming sites, AFGL 5180 and AFGL 6366S. This work includes a careful analysis of various data sets from NIR, mid-infrared, sub-millimeter, and centimeter wavelengths. It also includes the analysis of different molecular line data (i.e., ^{12}CO , ^{13}CO , and C^{18}O). The major observational outcomes of this work are as follows:

(i) AFGL 5180 and AFGL 6366S are nearby (distance $\sim 1.5 \text{ kpc}$) massive star-forming sites in their earlier stages. Both the sites host a Class II 6.7 GHz MME and reside at the opposite edges of an elongated filament F2, traced in dust continuum emission at the periphery of the H II region, S247.

(ii) Application of the *gtsf* utility on the *Herschel* 160 μm image reveals a HFS toward both the sites, hosting at least one 6.7 GHz MME. The radio continuum map at 8.46 GHz reveals a small cluster of radio sources in the vicinity of the central hub of the HFS toward AFGL 5180.

(iii) Based on the analysis of the photometric data at 1–5 μm , a total of 208 YSOs are identified toward our target area. The YSOs and outflow signatures are traced along the filament F2, which is further supported by the *Spitzer* ratio map. Clusters of YSOs are primarily depicted toward the edges of the filamentary cloud.

(iv) The filamentary cloud seems spatially close to the H II region, S247 excited by a massive O9.5 star, cgo115. Various pressure components exerted by the O-type star (i.e., $P_{\text{H II}}$, P_{rad} , and P_{wind}) on its surroundings are estimated. In this connection, the impact of the energetic feedback from the massive star on the filamentary cloud is found to be insignificant.

(v) Based on the analysis of molecular line data, previously proposed CCC scenario seems to be applicable in our target sites.

Overall, the collision of two clouds at $[-3.1, 4.8] \text{ km s}^{-1}$ and $[5.8, 12.9] \text{ km s}^{-1}$ had occurred about 1 Myr ago. Hence, the CCC process appears to explain the observed star formation activities (including massive stars) and HSFs. The filament connecting to sites AFGL 5180 and AFGL 6366S, can be a candidate of EDC. To further confirm the EDC process, high-resolution polarimetric and spectroscopic observations in sub-millimeter wavelengths will be helpful.

ACKNOWLEDGMENTS

We thank the anonymous referee for providing the valuable comments and suggestions, that improved the scientific content of this paper. The research work at Physical Research Laboratory is funded by the Department of Space, Government of India. We acknowledge F. Navarete for providing us with the narrow-band H₂ and K-band continuum images. This work is based [in part] on observations made with the *Spitzer* Space Telescope, which is operated by the Jet Propulsion Laboratory, California Institute of Technology, under a contract with NASA. This research made use of the data from the Milky Way Imaging Scroll Painting (MWISP) project, which is a multi-line survey in ¹²CO/¹³CO/C¹⁸O along the northern galactic plane with PMO-13.7m telescope. We are grateful to all the members of the MWISP working group, particularly the staff members at the PMO-13.7 m telescope, for their long-term support. MWISP was sponsored by National Key R&D Program of China with grant 2017YFA0402701 and by CAS Key Research Program of Frontier Sciences with grant QYZDJ-SSW-SLH047. This research has made use of the NASA/IPAC Infrared Science Archive, which is funded by the National Aeronautics and Space Administration and operated by the California Institute of Technology. The NVAS image was produced as part of the NRAO VLA Archive Survey, (c) AUI/NRAO. This research is based [in part] on observations made with the NASA/ESA Hubble Space Telescope obtained from the Space Telescope Science Institute, which is operated by the Association of Universities for Research in Astronomy, Inc., under NASA contract NAS 5–26555. These observations are associated with the proposal id 14465. This paper makes use of the following ALMA data: ADS/JAO.ALMA#2015.1.01454.S. ALMA is a partnership of ESO (representing its member states), NSF (USA) and NINS (Japan), together with NRC (Canada), MOST and ASIAA (Taiwan), and KASI (Republic of Korea), in cooperation with the Republic of Chile. The Joint ALMA Observatory is operated by ESO, AUI/NRAO and NAOJ. This research made use of *Astropy*¹, a community-developed core Python package for

Astronomy (*Astropy Collaboration et al.* 2013, 2018). For figures, we have used *matplotlib* (Hunter 2007) and IDL software.

Data availability

The *Herschel* and *Spitzer* data underlying this work are available in the publicly accessible NASA/IPAC infrared science archive². The K-band image is available in the UKIDSS-GPS survey³. The NVSS radio continuum image is available⁴. ALMA fits files utilized in this work are accessible from ALMA Data Archive⁵. *Gaia* EDR3 can be obtained from the publicly accessible server⁶. Distance of the *Gaia* EDR3 sources is available in the server⁷. HST NIR images are available in HST Data Archive⁸. NVAS radio continuum can be obtained from NRAO Data Archive⁹. *Planck* dust polarization data utilized in this work can be found in the publicly accessible server¹⁰.

REFERENCES

- Allamandola L. J., Tielens A. G. G. M., Barker J. R., 1989, *ApJS*, 71, 733
 Anathpindika S. V., 2010, *MNRAS*, 405, 1431
 André P., et al., 2010, *A&A*, 518, L102
 André P. J., Palmeirim P., Arzoumanian D., 2022, *A&A*, 667, L1
 Arzoumanian D., et al., 2021, *A&A*, 647, A78
 Astropy Collaboration et al., 2013, *A&A*, 558, A33
 Astropy Collaboration et al., 2018, *AJ*, 156, 123
 Bailer-Jones C. A. L., Rybizki J., Foesneau M., Demleitner M., Andrae R., 2021, *AJ*, 161, 147
 Balfour S. K., Whitworth A. P., Hubber D. A., Jaffa S. E., 2015, *MNRAS*, 453, 2471
 Bastien P., 1983, *A&A*, 119, 109
 Bertoldi F., 1989, *ApJ*, 346, 735
 Bhadari N. K., Dewangan L. K., Pirogov L. E., Ojha D. K., 2020, *ApJ*, 899, 167
 Bhadari N. K., Dewangan L. K., Zemlyanukha P. M., Ojha D. K., Zinchenko I. I., Sharma S., 2021, *ApJ*, 922, 207
 Bhadari N. K., Dewangan L. K., Ojha D. K., Pirogov L. E., Maity A. K., 2022, arXiv e-prints, p. arXiv:2204.00881
 Bik A., Kaper L., Hanson M. M., Smits M., 2005, *A&A*, 440, 121
 Bisbas T. G., Wünsch R., Whitworth A. P., Hubber D. A., 2009, *A&A*, 497, 649
 Breen S. L., Ellingsen S. P., Contreras Y., Green J. A., Caswell J. L., Stevens J. B., Dawson J. R., Voronkov M. A., 2013, *MNRAS*, 435, 524
 Bressert E., et al., 2010, *MNRAS*, 409, L54
 Bressert E., Ginsburg A., Bally J., Battersby C., Longmore S., Testi L., 2012, *ApJ*, 758, L28
 Carpenter J. M., Snell R. L., Schloerb F. P., Skrutskie M. F., 1993, *ApJ*, 407, 657
 Carpenter J. M., Snell R. L., Schloerb F. P., 1995a, *ApJ*, 445, 246
 Carpenter J. M., Snell R. L., Schloerb F. P., 1995b, *ApJ*, 450, 201
 Casali M., et al., 2007, *A&A*, 467, 777
 Casertano S., Hut P., 1985, *ApJ*, 298, 80
 Caswell J. L., Vaile R. A., Ellingsen S. P., Whiteoak J. B., Norris R. P., 1995, *MNRAS*, 272, 96

² <https://irsa.ipac.caltech.edu/frontpage/>

³ <http://wsa.roe.ac.uk/>

⁴ <https://skyview.gsfc.nasa.gov/current/cgi/query.pl>

⁵ <http://jvo.nao.ac.jp/portal/alma/archive.do>

⁶ <https://gea.esac.esa.int/archive/>

⁷ <https://vizier.cds.unistra.fr/viz-bin/VizieR?-source=I/352>

⁸ <https://www.cadc-ccda.hia-ihp.nrc-cnrc.gc.ca>

⁹ <https://science.nrao.edu>

¹⁰ <https://irsa.ipac.caltech.edu/applications/Planck/>

¹ <http://www.astropy.org>

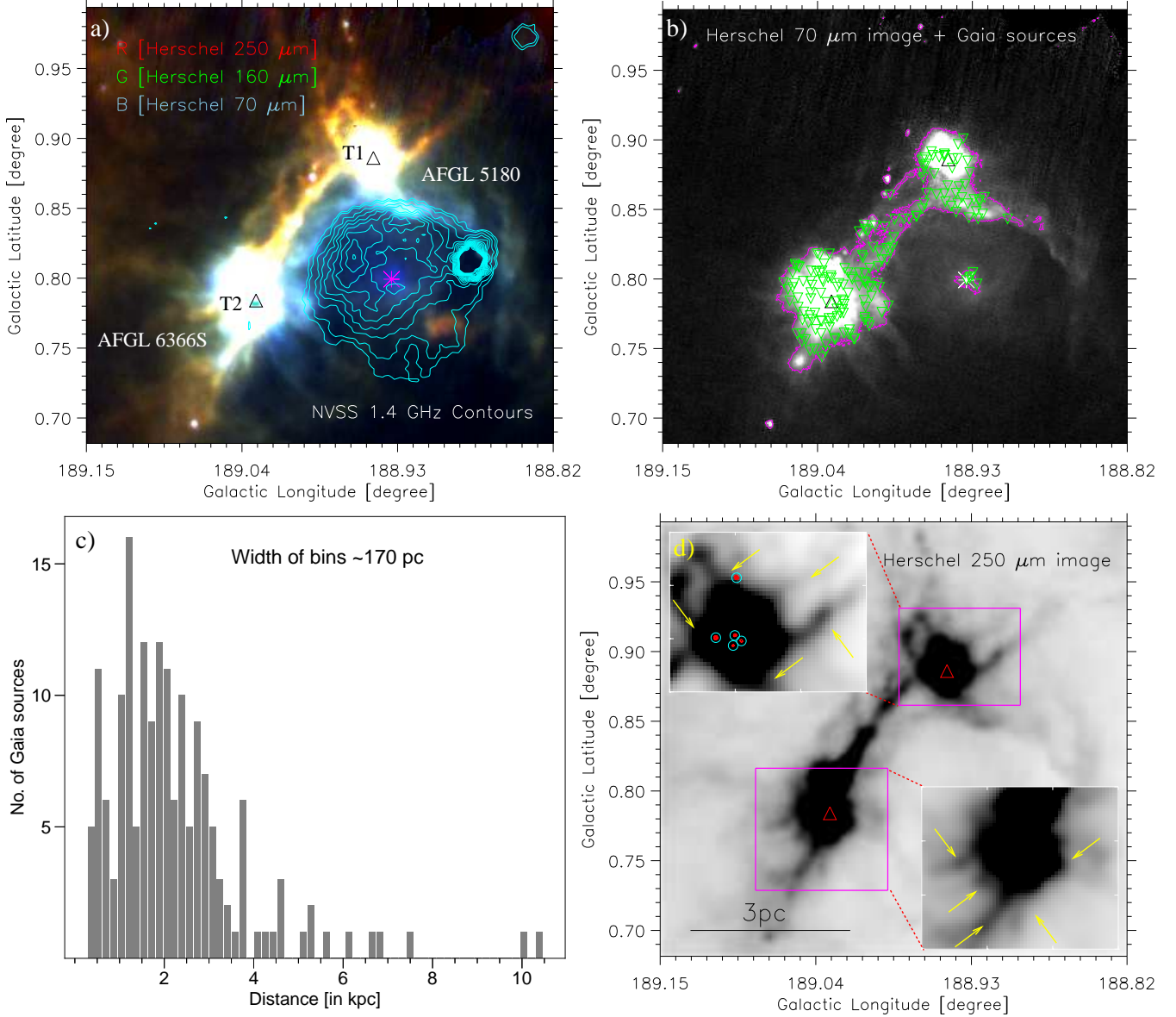


Figure 1. a) Overlay of the NVSS 1.4 GHz radio continuum emission contours on a three-color composite map of an area hosting AFGL 5180 and AFGL 6366S. The color composite map consists of the *Herschel* 250 μm image (in red), 160 μm image (in green), and 70 μm image (in blue). The NVSS radio continuum contours are plotted with levels of 3σ and 5σ to 80σ with an interval of 5σ , where $1\sigma \sim 0.45 \text{ mJy beam}^{-1}$. b) The panel shows the positions of the *Gaia* sources overlaid on the *Herschel* image at 70 μm (see upside down green triangles). The *Gaia* sources are mainly selected toward an elongated feature, which is indicated by a contour (in magenta) with a level of $0.06 \text{ Jy pixel}^{-1}$. c) The distance distribution of the selected *Gaia* sources. d) The panel shows the inverted grayscale *Herschel* image at 250 μm . The insets on the top-left and bottom-right present zoomed-in views of the sites AFGL 5180 (or T1) and AFGL 6366S (or T2), respectively, using the inverted grayscale *Herschel* image at 250 μm . In the direction of T1, the NVSS 8.46 GHz radio continuum contours at 120, 240, and 360 $\mu\text{Jy beam}^{-1}$ (where, $1\sigma \sim 36.8 \mu\text{Jy beam}^{-1}$) are shown in red. The peak positions of these radio continuum emissions are indicated by cyan circles (see the inset on the top-left). Arrows highlight sub-filaments toward both target sites. A scale bar of 3 pc is shown for a distance of 1.5 kpc. In panels “a”, “b” and “d” triangles indicate the positions of the 6.7 GHz MMEs. In “a” and “b”, the asterisk indicates the position of an O-type star, which is referred to as cgo115.

Chen Z., Nürnberg D. E. A., Chini R., Jiang Z., Fang M., 2015, *A&A*, **578**, A82
 Chung E. J., Lee C. W., Kwon W., Yoo H., Soam A., Cho J., 2022, arXiv e-prints, p. arXiv:2208.07891
 Churchwell E., 2002, *ARA&A*, **40**, 27
 Clarke S. D., Whitworth A. P., 2015, *MNRAS*, **449**, 1819
 Clarke S. D., Williams G. M., Walch S., 2020, *MNRAS*, **497**, 4390
 Condon J. J., Cotton W. D., Greisen E. W., Yin Q. F., Perley R. A., Taylor G. B., Broderick J. J., 1998, *AJ*, **115**, 1693
 Cox N. L. J., et al., 2016, *A&A*, **590**, A110
 Dale J. E., Bonnell I. A., Whitworth A. P., 2007, *MNRAS*, **375**, 1291

Dale J. E., Haworth T. J., Bressert E., 2015, *MNRAS*, **450**, 1199
 Davis C. J., Moriarty-Schieven G., Eisloffel J., Hoare M. G., Ray T. P., 1998, *AJ*, **115**, 1118
 Deharveng L., Zavagno A., Caplan J., 2005, *A&A*, **433**, 565
 Devine K. E., Churchwell E. B., Indebetouw R., Watson C., Crawford S. M., 2008, *AJ*, **135**, 2095
 Dewangan L. K., 2017, *ApJ*, **837**, 44
 Dewangan L. K., Ojha D. K., 2017, *ApJ*, **849**, 65
 Dewangan L. K., Ojha D. K., Zinchenko I., Janardhan P., Luna A., 2017a, *ApJ*, **834**, 22
 Dewangan L. K., Ojha D. K., Baug T., 2017b, *ApJ*, **844**, 15

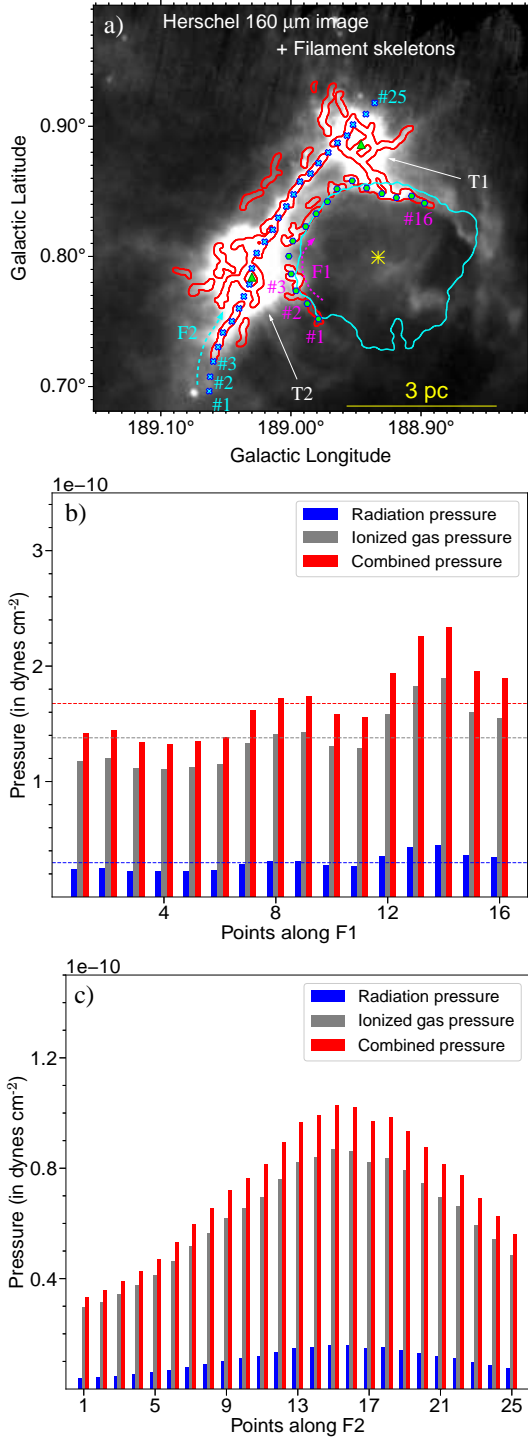


Figure 2. a) The panel shows the *Herschel* 160 μm continuum image overlaid with the NVSS 1.4 GHz radio continuum emission contour (in cyan) at $1.35 \text{ mJy beam}^{-1}$ and the filament skeletons (in red) identified using the *getsf* utility. The panel indicates two distinct structures: a curved feature F1 and an elongated filament F2. The filled hexagons and crosses mark several positions along F1 and F2 (see Section 3.1.3 for more details), respectively. These positions are also labeled in the panel. The asterisk and the triangles are the same as presented in Figure 1a. A scale bar representing 3 pc is also shown. b) The variation of radiation pressures (P_{rad} ; in blue), ionized gas pressures ($P_{\text{H II}}$; in gray), and combined pressures (i.e., $P_{\text{H II}} + P_{\text{rad}} + P_{\text{wind}}$; in red) computed at selected positions along F1, exerted by cgo115. The horizontal dashed lines indicate the average values of the pressure distributions. c) Same as Figure 2b, but it is shown for the positions along F2.

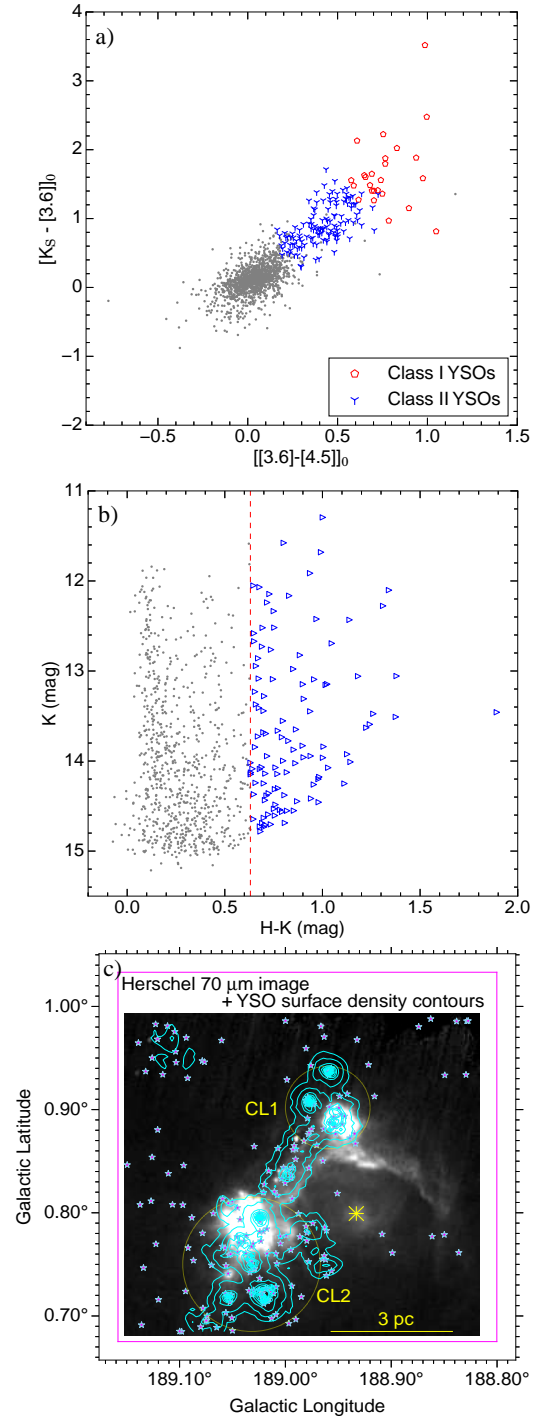


Figure 3. a) Dereddened color-color ($[[3.6] - [4.5]]_0$ Vs. $[K - [3.6]]_0$) diagram of point-like sources distributed toward our selected target area. Class I and Class II YSOs are indicated by pentagons (in red) and tri-down symbols (in blue), respectively. b) The panel shows the NIR color-magnitude ($H-K$ Vs. K) diagram of point-like sources (see Section 3.2 for details). Color-excess sources are highlighted by triangle-right symbols (in blue). c) Overlay of the positions of the selected YSO candidates (see magenta stars) on the *Herschel* 70 μm image. The surface density contours of YSOs are shown by cyan contours, and their levels are at 15, 25, 50, 75, 100, 125, 150, 175, 200, 225, 250, 275, and 300 YSOs pc^{-2} . The circles (in yellow) highlight the clusters of YSOs, which are found toward the edges of the filamentary structure. The scale bar and the asterisk are the same as Figure 2a. The magenta rectangle shows the area of the molecular data displayed in Figure 6.

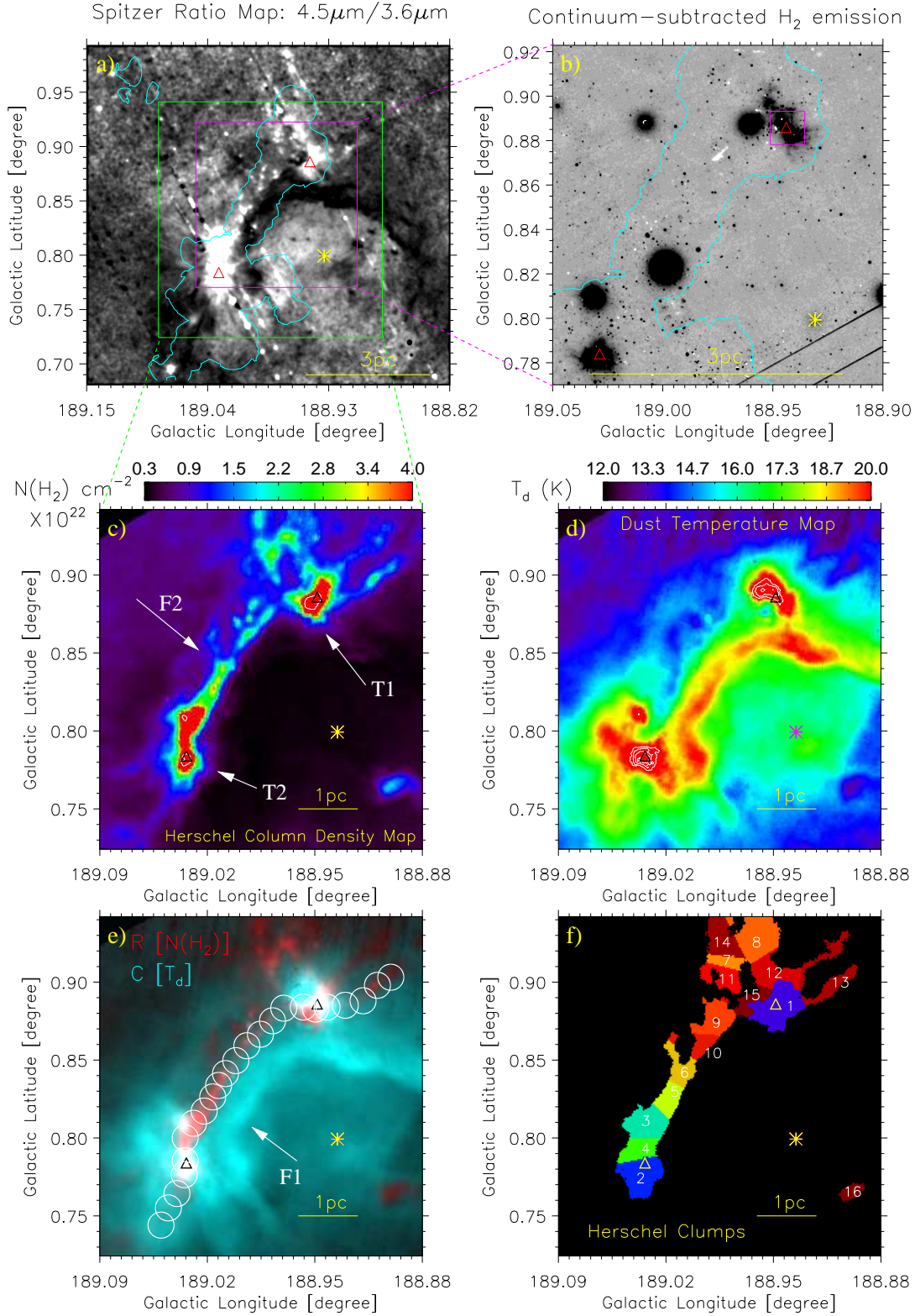


Figure 4. a) Overlay of the YSOs surface density contour at 15 YSOs pc^{-2} on the *Spitzer* ratio map (i.e., $4.5 \mu\text{m}/3.6 \mu\text{m}$). b) The panel shows the continuum-subtracted H_2 map (at $2.12 \mu\text{m}$) in grayscale for an area indicated by a magenta rectangle in Figure 4a. The magenta rectangle overlapped toward AFGL 5180 presents the area utilized for the zoomed-in view in Figure B1. c) The *Herschel* column density map (for an area indicated by a green rectangle in Figure 4a), overlapped with a white contour at the column density value of $10^{23} \text{ N}(\text{H}_2) \text{ cm}^{-2}$. d) The *Herschel* dust temperature map (for the same area as Figure 4c), overlaid with contours (in white) at the levels of 22, 24, and 26 K. e) A two-color composite image using the *Herschel* column density (in red) and dust temperature map (in cyan). Several circles (of radius $30''$) are also marked in the panel, where the average values of various physical parameters are computed (see Figure 7 and Section 3.5.1 for details). f) The panel shows the boundaries of the clumps identified in the *Herschel* column density map using the IDL-based algorithm *clumpfind*. The last four panels show a scale bar of 1 pc. Other symbols are identical to Figure 1a.

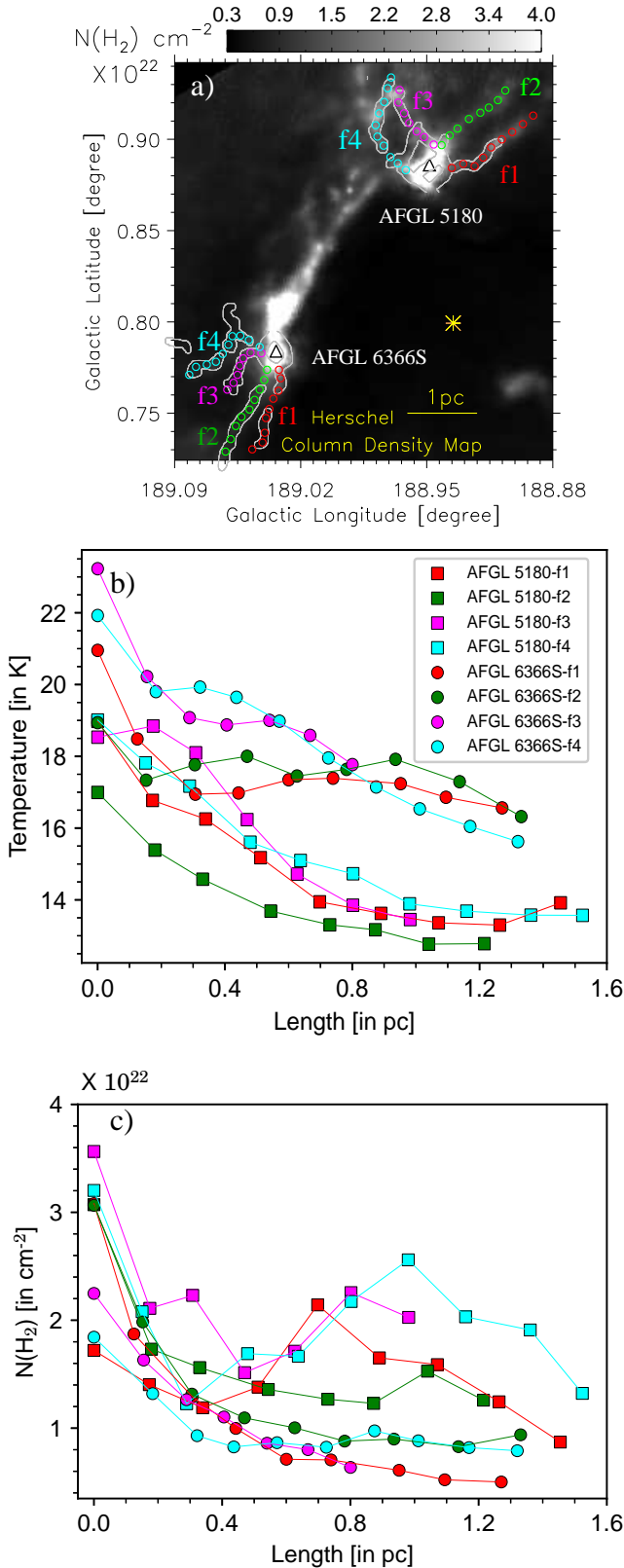


Figure 5. a) *Herschel* column density map identical as Figure 4c in grayscale. The sub-filaments (e.g., f1, f2, f3, and f4) both toward AFGL 5180 and AFGL 6366S are shown with gray contours. Other symbols are the same as Figure 4c. b) Distribution of the average dust temperature along the sub-filaments for the circular regions (of radius $7''$) overplotted on panel “a”. c) Distribution of the average column density along the sub-filaments for the same circular regions.

- Dewangan L. K., Pirogov L. E., Ryabukhina O. L., Ojha D. K., Zinchenko I., 2019, *ApJ*, **877**, 1
- Dewangan L. K., Sharma S., Pandey R., Palacio S. d., Ojha D. K., Benaglia P., Baug T., Das S. R., 2020a, *ApJ*, **898**, 172
- Dewangan L. K., Ojha D. K., Sharma S., Palacio S. d., Bhadari N. K., Das A., 2020b, *ApJ*, **903**, 13
- Dewangan L. K., Bhadari N. K., Maity A. K., Pandey R., Sharma S., Baug T., Eswaraiah C., 2022, arXiv e-prints, p. arXiv:2210.04658
- Dewangan L. K., Bhadari N. K., Men’shchikov A., Chung E. J., Devaraj R., Lee C. W., Maity A. K., Baug T., 2023, arXiv e-prints, p. arXiv:2302.07502
- Dobbs C. L., Pringle J. E., Duarte-Cabral A., 2015, *MNRAS*, **446**, 3608
- Draine B. T., 2003, *ARA&A*, **41**, 241
- Dyson J. E., Williams D. A., 1997, The physics of the interstellar medium, doi:10.1201/9780585368115.
- Elia D., et al., 2017, *MNRAS*, **471**, 100
- Elia D., et al., 2021, *MNRAS*, **504**, 2742
- Elmegreen B. G., Lada C. J., 1977, *ApJ*, **214**, 725
- Fedriani R., et al., 2019, *Nature Communications*, **10**, 4048
- Fujita S., et al., 2021, *PASJ*, **73**, S172
- Fukui Y., et al., 2014, *ApJ*, **780**, 36
- Fukui Y., et al., 2015, *ApJ*, **807**, L4
- Fukui Y., et al., 2018a, *PASJ*, **70**, S41
- Fukui Y., et al., 2018b, *ApJ*, **859**, 166
- Fukui Y., et al., 2019, *ApJ*, **886**, 14
- Fukui Y., Habe A., Inoue T., Enokiya R., Tachihara K., 2021a, *PASJ*, **73**, S1
- Fukui Y., Habe A., Inoue T., Enokiya R., Tachihara K., 2021b, *PASJ*, **73**, S1
- Gaia Collaboration et al., 2021, *A&A*, **649**, A1
- Ghosh S. K., Iyengar K. V. K., Karnik A. D., Rengarajan T. N., Tandon S. N., Verma R. P., 2000, Bulletin of the Astronomical Society of India, **28**, 515
- Gómez G. C., Vázquez-Semadeni E., Zamora-Avilés M., 2018, *MNRAS*, **480**, 2939
- Gutermuth R. A., Megeath S. T., Myers P. C., Allen L. E., Pipher J. L., Fazio G. G., 2009, *ApJS*, **184**, 18
- Habe A., Ohta K., 1992, *PASJ*, **44**, 203
- Hacar A., Alves J., Burkert A., Goldsmith P., 2016, *A&A*, **591**, A104
- Haworth T. J., Shima K., Tasker E. J., Fukui Y., Torii K., Dale J. E., Takahira K., Habe A., 2015, *MNRAS*, **454**, 1634
- Hayashi K., et al., 2018, *PASJ*, **70**, S48
- Hildebrand R. H., 1983, *QJRAS*, **24**, 267
- Hoare M. G., Kurtz S. E., Lizano S., Keto E., Hofner P., 2007, in Reipurth B., Jewitt D., Keil K., eds, Protostars and Planets V. p. 181 (arXiv:astro-ph/0603560)
- Hunter J. D., 2007, *Computing in Science and Engineering*, **9**, 90
- Klein R., Posselt B., Schreyer K., Forbrich J., Henning T., 2005, *ApJS*, **161**, 361
- Koempe C., Baudry A., Joncas G., Wouterloot J. G. A., 1989, *A&A*, **221**, 295
- Kumar M. S. N., Palmeirim P., Arzoumanian D., Inutsuka S. I., 2020, *A&A*, **642**, A87
- Kumar M. S. N., Arzoumanian D., Men’shchikov A., Palmeirim P., Matsumura M., Inutsuka S., 2022, *A&A*, **658**, A114
- Kurtz S., 2005, in Cesaroni R., Felli M., Churchwell E., Walmsley M., eds, Vol. 227, Massive Star Birth: A Crossroads of Astrophysics. pp 111–119, doi:10.1017/S1743921305004424
- Kurtz S., Churchwell E., Wood D. O. S., 1994, *ApJS*, **91**, 659
- Kwan J., 1997, *ApJ*, **489**, 284
- Lawrence A., et al., 2007, *MNRAS*, **379**, 1599
- Leistra A., Cotera A. S., Liebert J., 2006, *AJ*, **131**, 2571
- Long K. S., Blair W. P., Winkler P. F., Lacey C. K., 2020, *ApJ*, **899**, 14
- Lucas P. W., et al., 2008, *MNRAS*, **391**, 136
- Maity A. K., Dewangan L. K., Sano H., Tachihara K., Fukui Y., Bhadari N. K., 2022, *ApJ*, **934**, 2
- Marcolino W. L. F., Bouret J. C., Martins F., Hillier D. J., Lanz T., Escolano C., 2009, *A&A*, **498**, 837
- Martins F., Palacios A., 2017, *A&A*, **598**, A56
- Men’shchikov A., 2021, *A&A*, **649**, A89
- Menten K. M., 1991, *ApJ*, **380**, L75

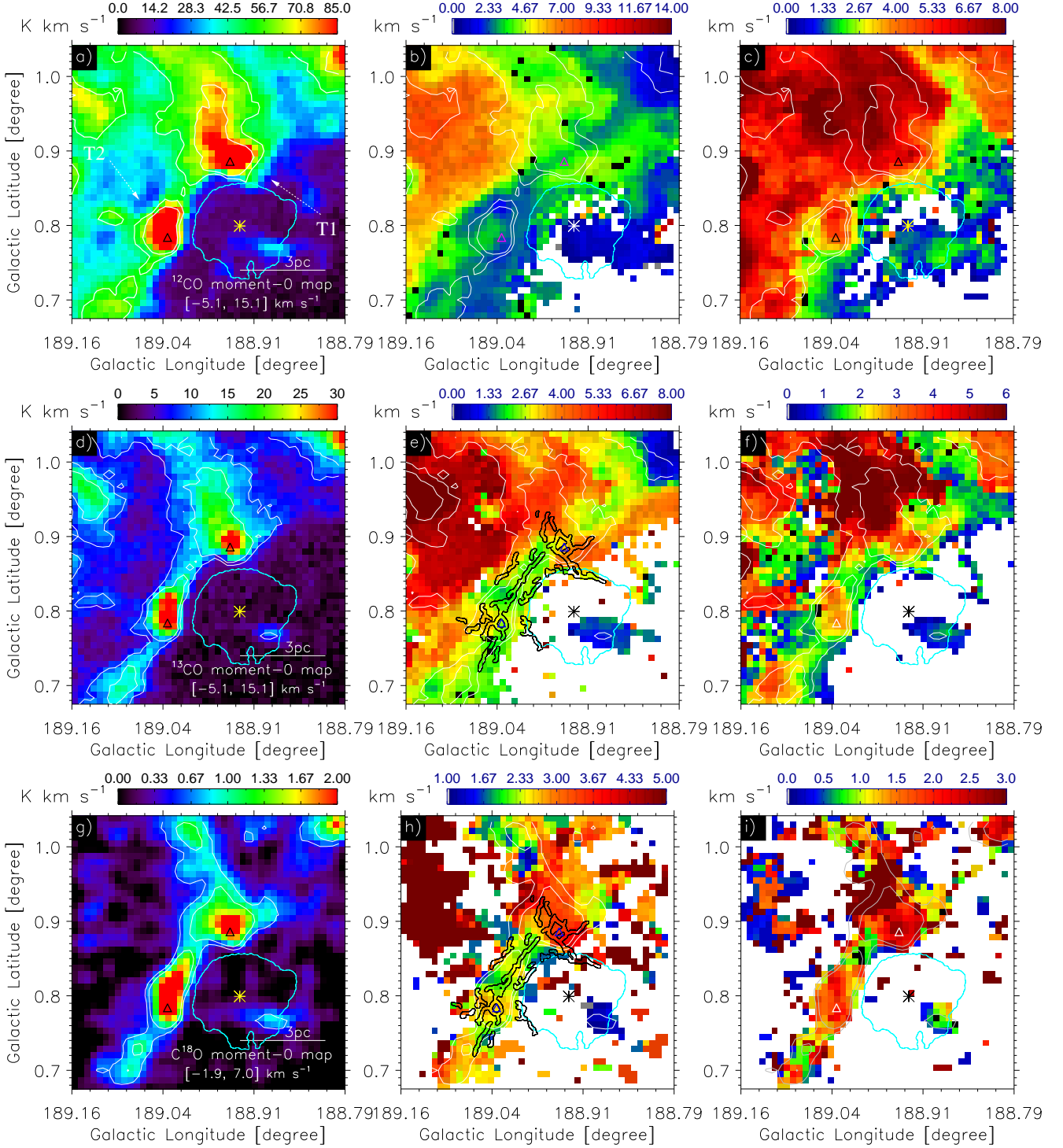


Figure 6. Moment maps of CO molecular line data. Moment-0 maps of a) ^{12}CO ; d) ^{13}CO ; g) C^{18}O . Moment-1 maps of b) ^{12}CO ; e) ^{13}CO ; h) C^{18}O . Linewidth (FWHM) maps of c) ^{12}CO ; f) ^{13}CO ; i) C^{18}O . All the moment maps of ^{12}CO (i.e., the top row) are overplotted with ^{12}CO integrated emission contours at 30% and 40% of the peak value (i.e., $\sim 174 \text{ K km s}^{-1}$). Similarly, the moment maps of ^{13}CO (i.e., the middle row) and C^{18}O (i.e., the bottom row) are overplotted with their integrated emission contours at 20% and 30% of corresponding peak values (i.e., $\sim 43 \text{ K km s}^{-1}$ and $\sim 3.3 \text{ K km s}^{-1}$, respectively). The moment-1 maps of ^{13}CO and C^{18}O emission are overlaid with the filament skeletons in black. The velocity ranges of integration are given in each moment-0 map. In all panels, the NVSS 1.4 GHz radio continuum contour at $1.35 \text{ mJy beam}^{-1}$ is also shown (in cyan), and other symbols are the same as shown in Figure 1a.

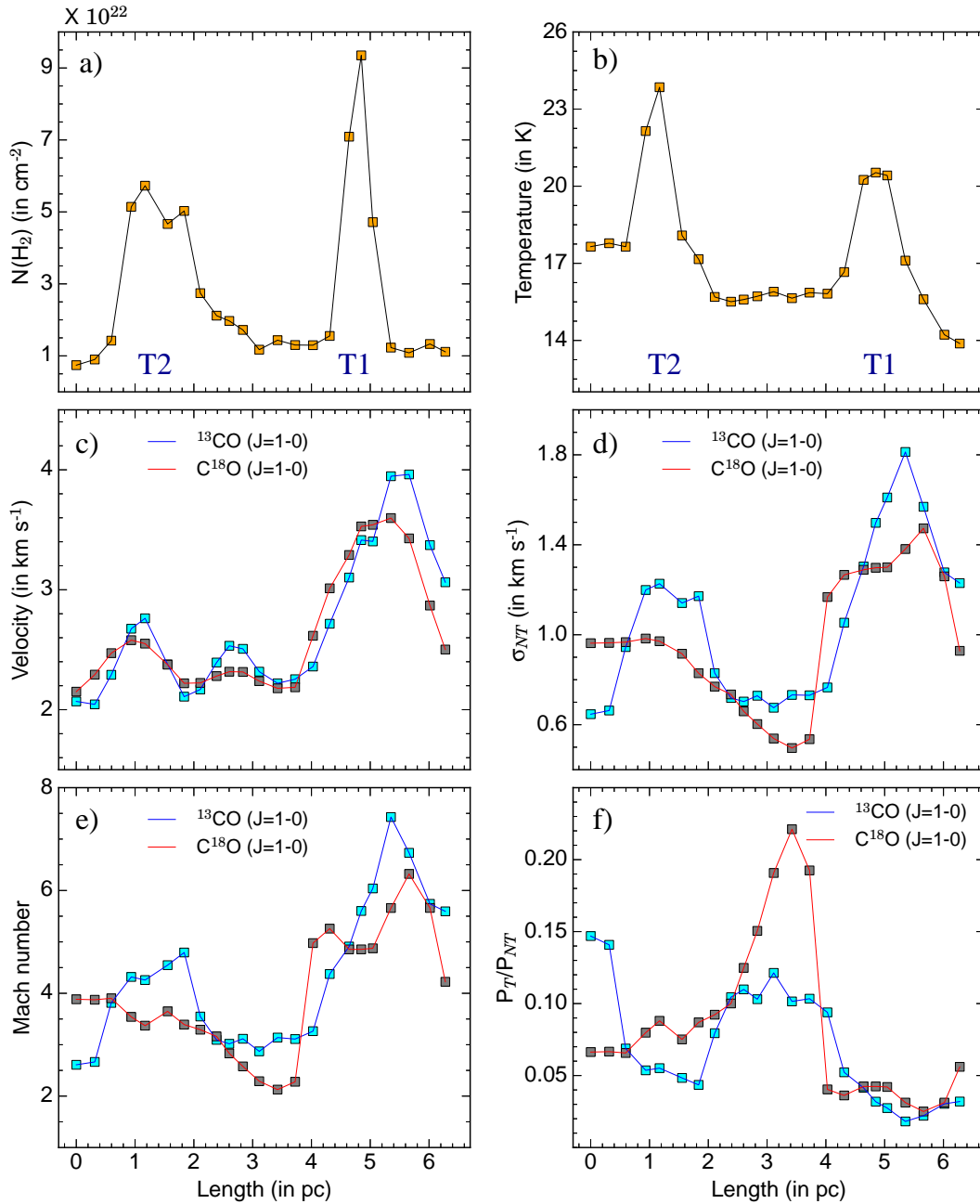


Figure 7. Distribution of a) average column density, b) average dust temperature, c) radial velocity, d) non-thermal velocity dispersion, e) Mach number, and f) ratio of thermal to non-thermal gas pressure for the circular regions shown in Figure 4e. In panels “c–f”, physical parameters are shown for ^{13}CO and C^{18}O line data.

Minier V., Conway J. E., Booth R. S., 2001, *A&A*, **369**, 278
Moffat A. F. J., Fitzgerald M. P., Jackson P. D., 1979, *A&AS*, **38**, 197
Molinari S., et al., 2010, *A&A*, **518**, L100
Motte F., Bontemps S., Louvet F., 2018, *ARA&A*, **56**, 41
Mutie M. M., Chibueze J. O., El Boucheffry K., MacLeod G. C., Morgan J., Baki P., 2021, *MNRAS*, **506**, 4175
Myers P. C., 2009, *ApJ*, **700**, 1609
Navarete F., Damineli A., Barbosa C. L., Blum R. D., 2015, *MNRAS*, **450**, 4364
Nishimura A., et al., 2017, arXiv e-prints, p. arXiv:1706.06002
Oh C. S., Kobayashi H., Honma M., Hirota T., Sato K., Ueno Y., 2010, *PASJ*, **62**, 101
Palmeirim P., et al., 2013, *A&A*, **550**, A38

Panagia N., 1973, *AJ*, **78**, 929
Pandey R., et al., 2020, *ApJ*, **891**, 81
Pety J., 2005, in Casoli F., Contini T., Hameury J. M., Pagani L., eds, SF2A-2005: Semaine de l’Astrophysique Francaise. p. 721
Phillips T. G., Huggins P. J., Wannier P. G., Scoville N. Z., 1979, *ApJ*, **231**, 720
Planck Collaboration et al., 2014, *A&A*, **571**, A1
Planck Collaboration et al., 2015, *A&A*, **576**, A104
Planck Collaboration et al., 2016a, *A&A*, **586**, A136
Planck Collaboration et al., 2016b, *A&A*, **586**, A138
Planck Collaboration et al., 2016c, *A&A*, **594**, A19
Pon A., Toalá J. A., Johnstone D., Vázquez-Semadeni E., Heitsch F., Gómez G. C., 2012, *ApJ*, **756**, 145

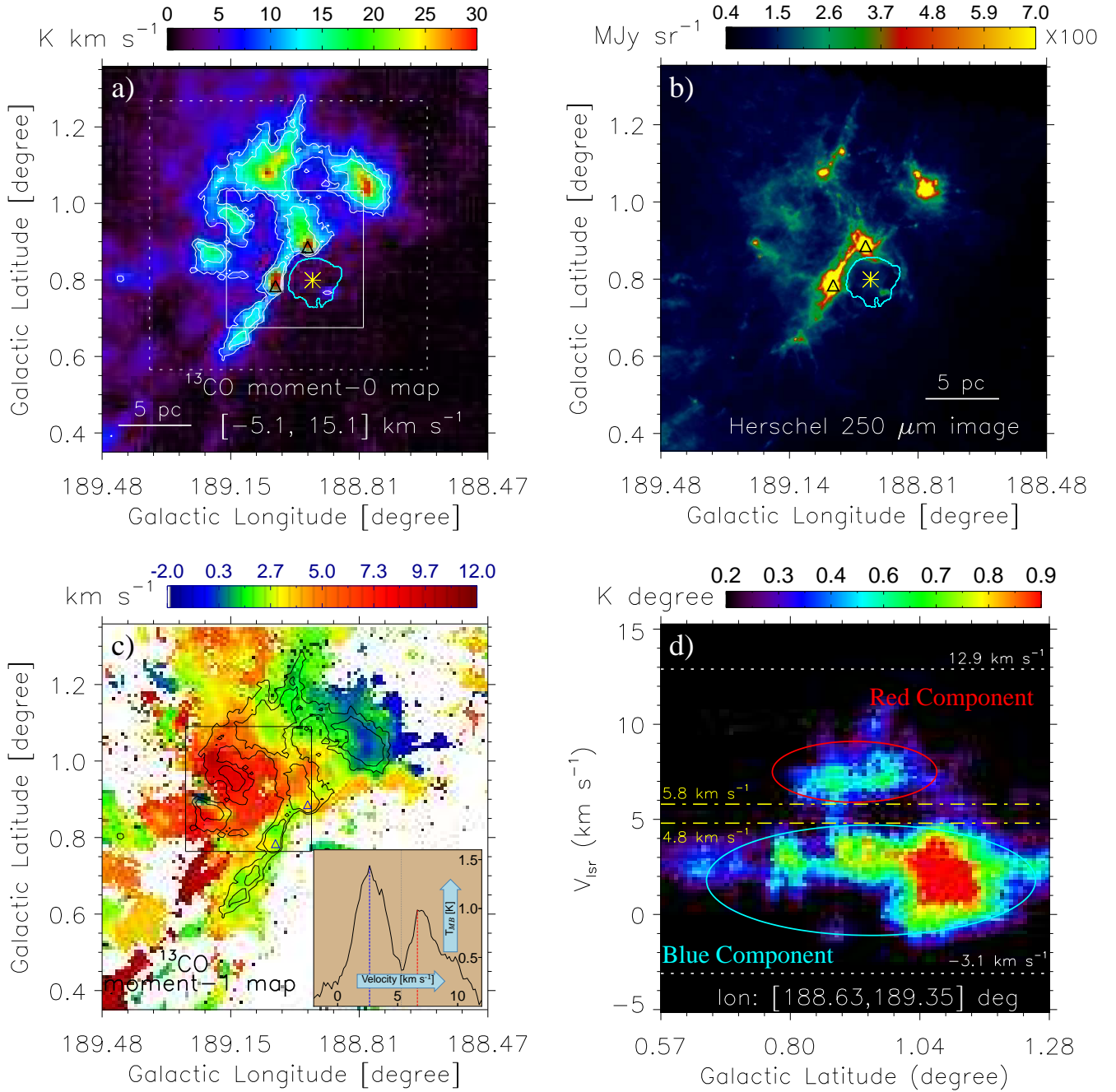


Figure 8. a) Moment-0 map of ^{13}CO emission toward our target sites for an extended area of about $60' \times 60'$ and a velocity integration range $[-5.1, 15.1] \text{ km s}^{-1}$. The contours are at the 20% and 30% of the peak value (i.e., $\sim 43 \text{ K km s}^{-1}$). A scale bar of 5 pc is shown along with other symbols identical to Figure 6. The white rectangle (solid) presents the area of the molecular data shown in Figure 6. The white rectangle (dotted) indicates the area of the molecular data utilized for the Galactic latitude-velocity diagram shown in Figure 8d. b) *Herschel* 250 μm dust continuum image for the same region as Figure 8a. c) Moment-1 map of ^{13}CO data with identical contours as in Figure 8a. The black rectangle presents the area utilized to extract the average intensity profile, which is shown in the inset. d) Galactic latitude-velocity diagram for Galactic longitude integration range $[188.63, 189.35]$ degree. The dashed and dotted horizontal lines present different V_{lsr} values, as the figure mentions. The cyan and red ellipses show the blue-shifted and red-shifted cloud components, respectively.

Povich M. S., et al., 2007, *ApJ*, 660, 346
 Priestley F. D., Whitworth A. P., 2021, *MNRAS*, 506, 775
 Reid M. J., Menten K. M., Brunthaler A., Zheng X. W., Moscadelli L., Xu Y., 2009, *ApJ*, 693, 397
 Roman-Lopes A., Roman-Lopes G. F., 2019, *MNRAS*, 484, 5578
 Rosen A. L., Offner S. S. R., Sadavoy S. I., Bhandare A., Vázquez-Semadeni E., Ginsburg A., 2020, *Space Sci. Rev.*, 216, 62
 Saito H., Saito M., Sunada K., Yonekura Y., 2007, *ApJ*, 659, 459

Sano H., et al., 2017, arXiv e-prints, p. arXiv:1708.08149
 Sano H., et al., 2018, *PASJ*, 70, S43
 Schneider N., et al., 2012, *A&A*, 540, L11
 Sharpless S., 1959, *ApJS*, 4, 257
 Shimoikura T., et al., 2013, *ApJ*, 768, 72
 Skrutskie M. F., et al., 2006, *AJ*, 131, 1163
 Soubie T., 2011, *MNRAS*, 414, 350
 Su Y., et al., 2019, *ApJS*, 240, 9

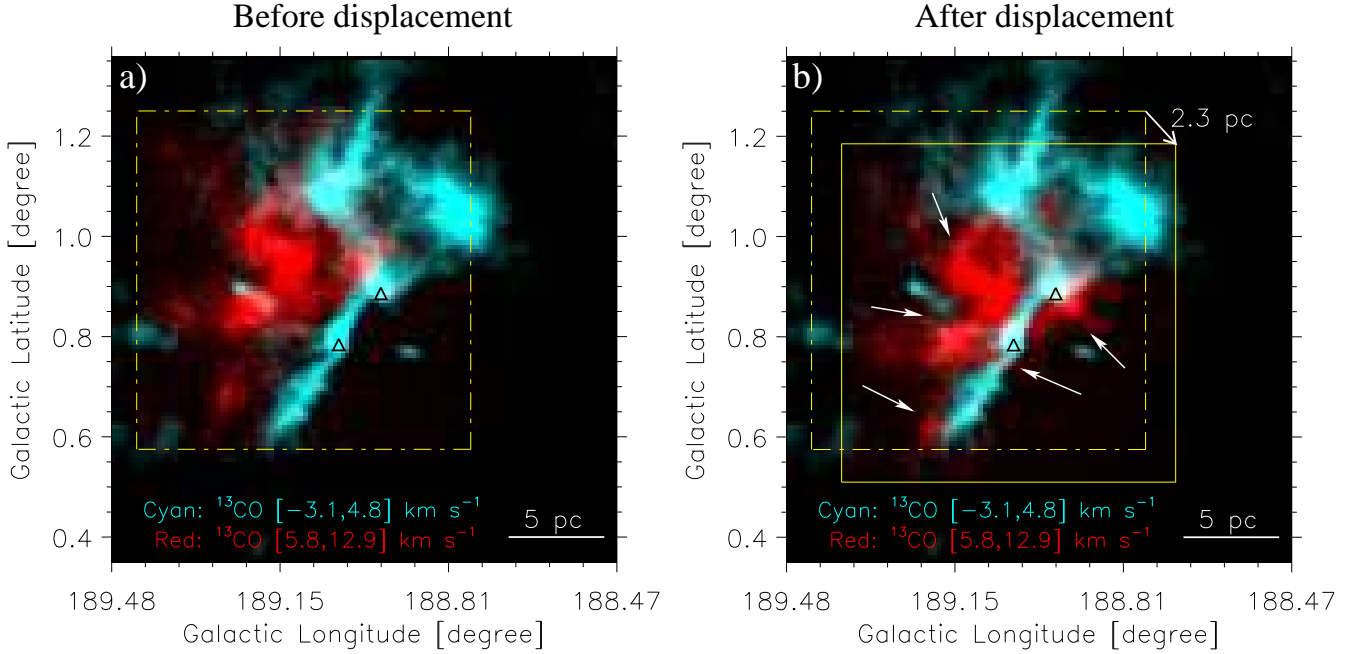


Figure 9. a) A two-color composite image shows the spatial distribution of the blue and red cloud components. The moment-0 map for the blue component is displayed in cyan on the linear scale from 2 to 14 K km s⁻¹. Similarly, the moment-0 map for the red component is shown in red, ranging from 0 to 8 K km s⁻¹ on the linear scale within the yellow dashed rectangle. b) Spatial distribution of the blue and red cloud components with a spatial shift of about 2.3 pc. The dashed and solid yellow rectangle presents the initial and final positions of the red cloud component, respectively. The white arrows overlaid indicate toward the complementary distribution between the cloud components. The velocity integration ranges for the blue and red cloud components are specified in both the panels. The scale bar and other symbols are identical to Figure 8a.

- Sun J. X., Lu D. R., Yang J., Su Y., Zhang S. B., Zhou X., Lin Z. H., 2018, *Acta Astronomica Sinica*, **59**, 3
- Szymczak M., Olech M., Sarniak R., Wolak P., Bartkiewicz A., 2018, *MNRAS*, **474**, 219
- Tan J. C., Beltrán M. T., Caselli P., Fontani F., Fuente A., Krumholz M. R., McKee C. F., Stolte A., 2014, in Beuther H., Klessen R. S., Dullemond C. P., Henning T., eds, *Protostars and Planets VI*. p. 149 ([arXiv:1402.0919](https://arxiv.org/abs/1402.0919)), [doi:10.2458/azu_uapress_9780816531240-ch007](https://doi.org/10.2458/azu_uapress_9780816531240-ch007)
- Tasker E. J., Tan J. C., 2009, *ApJ*, **700**, 358
- Tielens A. G. G. M., 2008, *ARA&A*, **46**, 289
- Tigé J., et al., 2017, *A&A*, **602**, A77
- Tokuda K., et al., 2019, *ApJ*, **886**, 15
- Torii K., et al., 2011, *ApJ*, **738**, 46
- Torii K., et al., 2015, *ApJ*, **806**, 7
- Torii K., et al., 2017, *ApJ*, **835**, 142
- Torii K., et al., 2021, *PASJ*, **73**, S368
- Tremblin P., et al., 2014, *A&A*, **568**, A4
- Treviño-Morales S. P., et al., 2019, *A&A*, **629**, A81
- Vasyunina T., 2010, PhD thesis, Ruprecht-Karls University of Heidelberg, Germany
- Walsh A. J., Burton M. G., Hyland A. R., Robinson G., 1998, *MNRAS*, **301**, 640
- Wang J.-W., et al., 2019, *ApJ*, **876**, 42
- Weingartner J. C., Draine B. T., 2001, *ApJ*, **548**, 296
- Whitney B., et al., 2011, in *American Astronomical Society Meeting Abstracts #217*. p. 241.16
- Williams J. P., de Geus E. J., Blitz L., 1994, *ApJ*, **428**, 693
- Wu Y. W., Xu Y., Pandian J. D., Yang J., Henkel C., Menten K. M., Zhang S. B., 2010, *ApJ*, **720**, 392
- Yang A. Y., et al., 2021, *A&A*, **645**, A110
- Yang A. Y., et al., 2022, *A&A*, **658**, A160
- Yuan L., et al., 2020, *A&A*, **637**, A67
- Zernicke A., Schilke P., Smith R. J., 2013, *A&A*, **554**, L2

Zinnecker H., Yorke H. W., 2007, *ARA&A*, **45**, 481

APPENDIX A: PLANE OF SKY MAGNETIC FIELD IN OUR TARGET AREA

We derived the plane-of-sky (POS) magnetic field position angles using the *Planck* 353 GHz Stokes I, Q, and U images. We first estimated the linear polarization angles (PAs) of dust emission in Galactic coordinates using the conventional relation of $\theta_{\text{GAL}} = 0.5 \times \arctan2(-U, Q)$. The negative sign in U is used to follow the IAU convention (see more details in [Planck Collaboration et al. 2015](#)) and a two-argument function $\arctan2$ is used to avoid the π -ambiguity in the estimation of PAs. The magnetic field orientations (B_{Gal}) were then computed by adding 90° in the electric field PAs (e.g., [Planck Collaboration et al. 2016a,c](#)). B_{Gal} is measured from the Galactic north to the anticlockwise direction (i.e., toward east).

Figure A1a displays the *Planck* 353 GHz image of our target site. The distribution of the POS magnetic field is shown by the overlaid pseudo-vectors in Figure A1a. The magnetic field direction is nearly perpendicular to the filament, consistent with the observations of other targets (e.g., [Palmeirim et al. 2013](#); [Planck Collaboration et al. 2016b](#); [Cox et al. 2016](#)). The spatial distribution of B_{Gal} is shown in Figure A1b. We have also studied the variation of magnetic field position angle with respect to the filament's major axis (i.e., B_{Filament}). The variation of B_{Gal} and B_{Filament} toward our target area is shown in Figure A1c. A linear trend in B_{Filament} along filament's major axis hint at longitudinal mass flow from the edges toward the central part ([Dewangan et al. 2023](#)). However, new high-resolution dust polarization data toward

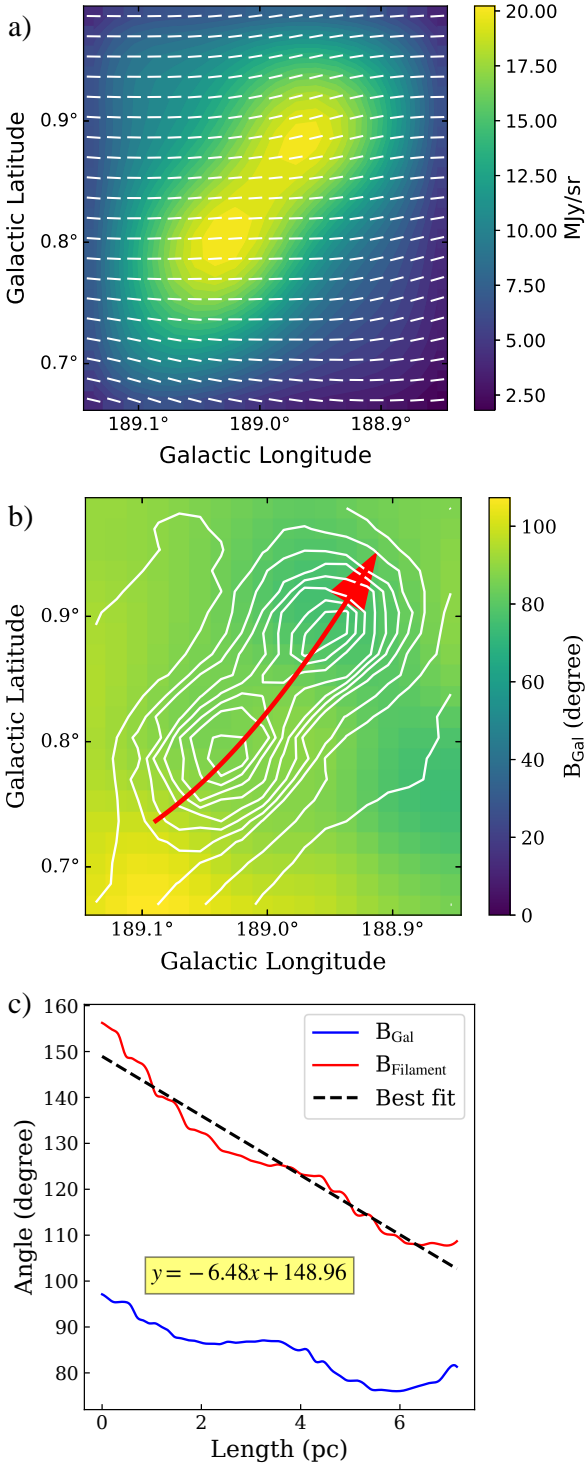


Figure A1. a) The *Planck* 353 GHz map of our target area (see the white dotted rectangle in Figure 9a) overlaid by the POS magnetic field pseudo-vectors. b) Spatial distribution of the POS magnetic field position angle measured from Galactic north to the anticlockwise direction (B_{Gal}). The overlaid contours indicate the *Planck* 353 GHz intensity ranging from 4.6 to 27.6 MJy sr $^{-1}$ in linear order. c) Distribution of B_{Gal} and B_{Filament} along the red curved arrow shown in panel “b”. B_{Filament} is the magnetic field position angle measured from filament’s major axis (see text in Appendix A for more details). A best-fitted line is displayed and labeled for the B_{Filament} distribution.

our target area can shed more light on the role of the magnetic field on the observed morphology.

APPENDIX B: A ZOOMED-IN VIEW OF MASSIVE STAR-FORMING REGION T1

UKIDSS and HST high-resolution NIR images allow us to examine a zoom-in view of T1 (see the magenta rectangle in Figure 4b). In Figure B1a, we present a two-color composite image (based on UKIDSS K band image in red and HST F160W band image in cyan), overlaid with the NVAS 8.46 GHz radio continuum emission contours in green, showing the presence of three compact radio sources toward the site AFGL 5180. Ionized areas smaller than 0.05 pc in size are previously referred to as the HC H II regions (Yang et al. 2021), which are younger than the UC H II regions. Toward AFGL 5180 one of the radio continuum sources is exclusively associated with the Class II 6.7 GHz MME. Other radio sources lack detection of the 6.7 GHz MME, and one of them (at the top) spatially coexists with a B4V-B8V spectral type star (Vasunina 2010).

Following the method described in Long et al. (2020), the continuum-subtracted [Fe II] image at 1.64 μm is produced using the HST F164N and F160W band images. The shock-excited materials due to outflows and jets are the sources of [Fe II] emissions in star-forming regions (Fedriani et al. 2019). In the direction of T1, we have displayed the continuum-subtracted [Fe II] emission at 1.64 μm with the help of red contours on the HST F110W band image (see Figure B1b). Interestingly, the 6.7 GHz MME and the NVAS 8.46 GHz radio continuum emission are detected at the center of the bipolar morphology (or the bipolar outflow).

The area highlighted by a cyan box in Figure B1b is further zoomed-in using the ALMA 1.3 mm dust continuum emission (resolution $\sim 0''.18 \times 0''.28$), and is presented in Figure B1c. The presence of at least two cores (i.e., core-1 and core-2) is evident in Figure B1c. The cyan arrow indicates an extended dust emission surrounding one of the cores. The pink arrows point out the candidate cores residing on the line joining the primary cores. Using the formula of Hildebrand (1983) (see Equation 3 in Mutie et al. 2021), we obtained the masses of the core-1 and core-2 to be about 5.4 M_{\odot} and 1.3 M_{\odot} , respectively. We have chosen 6σ as the contour value to evaluate the total dust emissions using the *clumpfind*. The distance and the temperature of the source are taken to be 1.5 kpc and 25 K, respectively. The gas-to-dust ratio and the opacity value are adopted to be 100 and 0.33 cm 2 g $^{-1}$, respectively (Weingartner & Draine 2001; Mutie et al. 2021). Additionally, the mass of the elongated envelope around core 2 is determined to be about 1.1 M_{\odot} . Earlier, Mutie et al. (2021) reported the mass of the core-1 and core-2 to be 8.2 M_{\odot} and 4.8 M_{\odot} , which are different from our estimations. The difference with our estimated mass values mainly arises due to the use of the different values of distance and temperature. The core-1 and core-2 traced in the ALMA 1.3 mm continuum emission map (resolution $\sim 0''.18 \times 0''.28$) are presented in Figure B1d. We have also shown the 1.3 mm continuum emission (resolution $\sim 0''.63 \times 1''.23$) contours (in red), the NVAS 8.46 GHz radio continuum emission contours (in black), and the position of the 6.7 GHz MME in Figure B1d. In Figure B1d, we find that the core-1 is associated with the 6.7 GHz MME and the radio continuum emission. The core-1 (mass $\sim 5.4 M_{\odot}$) is connected with the core-2 (mass $\sim 1.3 M_{\odot}$) by the dust emission (extent < 5000 AU), showing a dumbbell-like configuration at small scale. Such configuration is traced within the

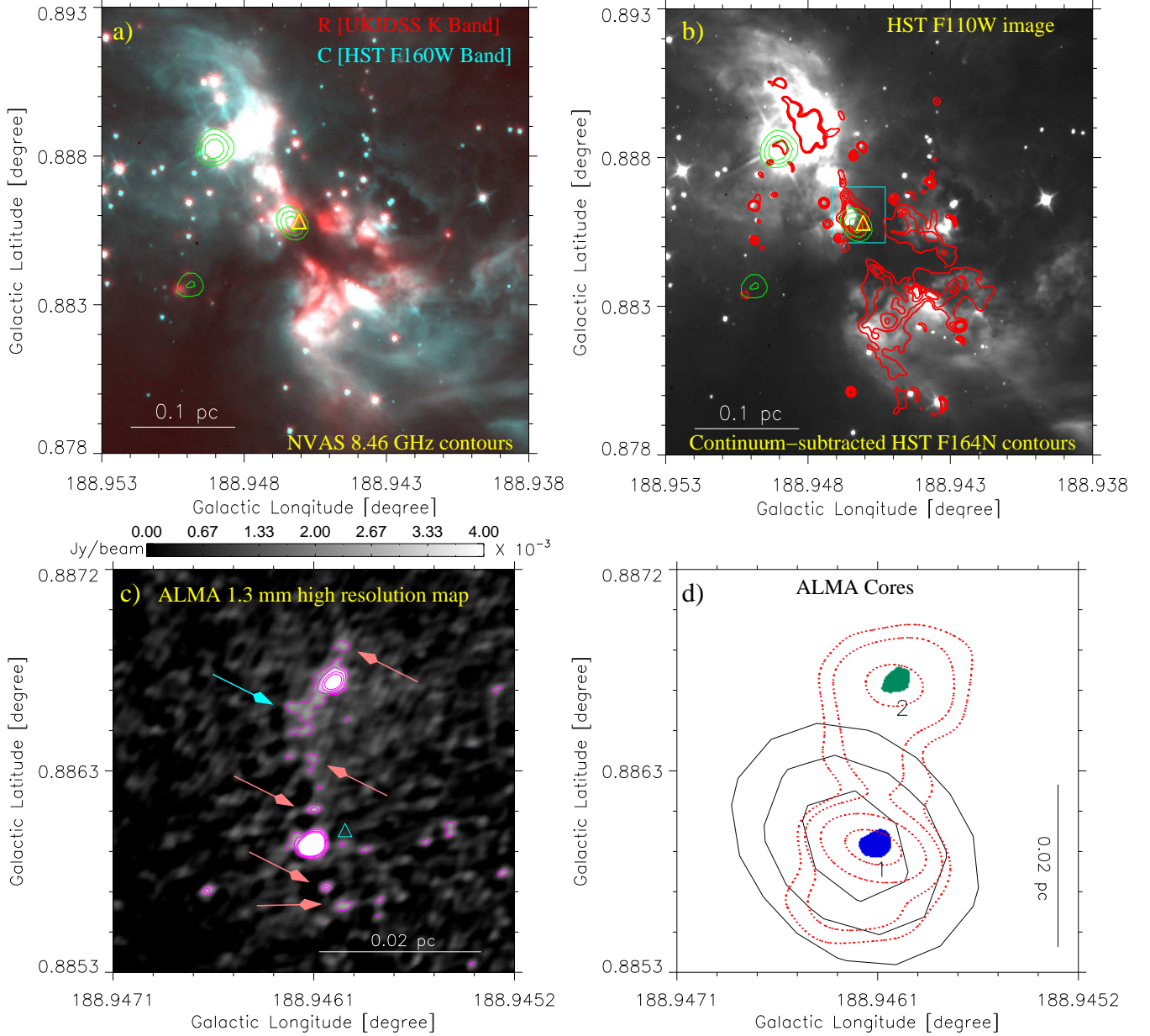


Figure B1. a) A zoomed-in view of the site AFGL 5180 (for a rectangular area shown in Figure 4b) using a two-color composite image (UKIDSS K-band image in red + HST F160W band image in cyan). The NVAS 8.46 GHz radio continuum emission contours (in green) are also overlaid on the color composite image. b) The panel presents the HST F110W wide band image overplotted with the continuum-subtracted [Fe II] emission contours (at 1.64 μm ; in red) and the NVAS 8.46 GHz radio continuum emission contours (in green). c) The panel presents the ALMA 1.3 mm dust continuum emission map (resolution $\sim 0''.18 \times 0''.28$) of an area highlighted by a rectangle in Figure B1b. The 1.3 mm dust continuum emission contours are shown at values 4σ , 6σ , 9σ and 12σ , where $1\sigma = 0.45 \text{ mJy beam}^{-1}$. The arrows indicate possible low-mass cores and an envelope-like feature (see Appendix B for more details). d) The panel shows the positions of two cores (i.e., 1 and 2) detected in the ALMA 1.3 mm dust continuum map (resolution $\sim 0''.18 \times 0''.28$). The NVAS 8.46 GHz radio continuum emission contours are also plotted in black (see Figure B1a). The dotted contours in red show the 1.3 mm dust continuum emission (resolution $\sim 0''.63 \times 1''.23$) with the levels of 8, 14, 20, 26, and 32 mJy beam^{-1} . In panels "a", "b" and "c", the triangle indicates the position of the 6.7 GHz MME, and the radio continuum contours are plotted with the levels of 120, 160, and $200 \mu\text{Jy beam}^{-1}$, where $1\sigma = 36.8 \mu\text{Jy beam}^{-1}$. A scale bar of 0.1 pc and 0.02 pc is shown in panels ("a", "b") and ("c", "d"), respectively.

central hub of the HFS in AFGL 5180. One can also notice that no radio continuum emission is seen toward the core-2.